Fabrication of a gap structure for near-field heat transfer

Master's thesis, 27.11.2016

Author:
Samuli Heiskanen

Supervisor:
Ilari Maasilta

ACKNOWLEDGMENTS

Finally I am writing this thesis after a long time of studying. These four and a half years of hard work are coming to their conclusion and I am happy of what I have achieved. Not only has it been a long time of studying but also this near-field project has been going on for three summers and now I finally get to write my master's thesis about the project. Even though this was a long project I am happy that I got to do it because nanofabrication is exactly what I wanted to do when I came here to study nanosciences. However this is hopefully not the end of my studies or research since I am hoping to continue as a postgraduate student here at the University of Jyväskylä.

I would like to especially thank my instructors Ilari Maasilta and Geng Zhuoran who have helped me with this project for three years. Special thanks go to Ilari for asking me to come to work in his group in the summer after my second year even though I had not even applied for the summer jobs in the department of physics. Other people who helped me with this project were Andrii Torgovkin, Yaolan Tian, Michael Savytskyi and Teemu Loippo and I want to thank them all for their help. Also I want to thank anyone who takes the time to read this thesis. I hope that you find the results of my work helpful.

Jyväskylä September, 2016

Samuli Heiskanen

ABSTRACT

Heiskanen, Samuli
Fabrication of a gap structure for near-field heat transfer
Master's thesis
Department of Physics, University of Jyväskylä, 2016, 56 pages.

A two-step fabrication process for a gap structure with metal wiring was developed in this study. This gap structure is meant to be used for near field heat transfer measurements. The fabrication was mostly done with 3D-lithography using a Nanoscribe Photonic Professional system. The fabrication also included ALD (Atomic Layer Deposition), metal coating by evaporation, lift-off and ion beam milling. The fabricated structure consists of two cuboids close together which form a suspended parallel plate geometry. The metallizations fabricated on the cuboids consist of a thin gold wire which can work as a resistive thermometer and a heater. The fabrication process was successfully developed and a gap size of (1.97 ± 0.05) µm was reached. The biggest issues with the fabrication were the tension in the 3D structures which limits the gap size and the difficulty of the lift-off process needed for the metallizations. Very often the structures broke or extra gold film was left on the structures. Measurements were also performed, which showed that the fabricated wires can in fact work as a heater and as a thermometer down to a temperature of about 25 K.

Keywords: Near-field, 3D-lithography, nanofabrication, structure

TIIVISTELMÄ

Heiskanen, Samuli
Rakorakenteen valmistaminen lähikentän lämmönsiirtymistä varten
Pro gradu
Fysiikan laitos, Jyväskylän yliopisto, 2016, 56 sivua.

Tutkimuksessa kehitettiin kahden vaiheen valmistusprosessi rakorakenteen valmistamiseen, jossa on metallista valmistetut johdot. Tämä rakorakenne on tarkoitettu lähikentän lämmönsiirtymisen mittaamiseen. Valmistus tehtiin pääasiassa 3D-litografialla käyttämällä Nanoscribe Photonic Professional -järjestelmää. Valmistukseen sisältyi myös ALD (Atomic Layer Deposition), metallipäällystys höyrystämällä, lift-off ja ionisuihkujyrsintä. Valmistettu rakenne koostuu kahdesta suorakulmaisesta särmiöstä lähellä toisiaan, jotka muodostavat ripustetun yhdensuuntaisten tasojen geometrian. Särmiöiden päälle tehdyt metalloinnit koostuivat ohuesta kultalangasta, joka voi toimia resistiivisenä lämpömittarina ja lämmittimenä. Valmistusprosessi kehitettiin onnistuneesti ja (1.97 ± 0.05) µm leveä rako saavutettiin. Suurimmat ongelmat valmistuksessa olivat jännitys 3D rakenteissa, joka rajoittaa raon kokoa, ja metalloinneille tarvitun lift-off -prosessin vaikeus. Usein rakenteet hajosivat tai ylimääräistä kultakalvoa jäi rakenteiden päälle. Lisäksi tehtiin mittauksia, jotka osoittivat että valmistetut langat voivat toimia lämmittimenä ja lämpömittarina suuremmissa lämpötiloissa kuin 25 K.

Avainsanat: Lähikenttä, 3D-litografia, nanovalmistus, rakenne

CONTENTS

1 Introduction **6**

2 Theoretical background **8**
2.1 Near-field heat transfer 8
2.2 Review of previous near field experimental set-ups 13
2.3 Fabrication methods 15
2.3.1 3D-lithography 15
2.3.2 Atomic layer deposition 17
2.3.3 Helium ion microscopy and milling 19
2.3.4 Physical vapor deposition 20

3 Materials and methods **22**
3.1 Sample fabrication 22
3.1.1 Design 22
3.1.2 Lithography for the base structures 23
3.1.3 Coating the base structures with aluminium oxide 24
3.1.4 Coating the base structures with a resist 25
3.1.5 Lithography for the wiring 25
3.1.6 Evaporation and lift-off 26
3.1.7 Imaging and ion beam milling 27
3.2 Measurement setups 29
3.2.1 Probe station 29
3.2.2 Dip stick 30

4 Earlier Results **33**

5 Results **35**
5.1 The wiring lithography process 35
5.2 Coating a fabricated structure with resist 37
5.3 Metal deposition and lift-off on a fabricated structure 40
5.4 Making the gap smaller with ion beam milling 44
5.5 Resistance measurements with the probe station 46
5.6 Dip stick measurements 49

6 Conclusion **52**

References **54**

1 INTRODUCTION

The black body theory for heat radiation developed by Max Planck gives a limit for the maximum amount of heat that can transfer radiatively between two bodies [1]. However if two bodies are brought close enough together, the hotter body can start heating the colder body through evanescent coupling of thermally excited electromagnetic surface waves. This distance has to be in the nanometre range at room temperature for this effect to happen. In this near-field regime the heat transfer can exceed the Planck law with many orders of magnitude. In this regime the amount of heat transfer increases when the distance between the two bodies gets smaller and also the geometry of the bodies has a large effect on the heat transfer [2]. The theory of this effect has been well studied in the simplest geometries, but it is very hard to study it experimentally due to the very small gap that is needed. Only very recently many studies have been made in this field because better fabrication techniques have been developed [3]-[10]. These experiments seem to agree with the theory and show that a small enough gap can be reached with today's fabrication techniques to see a large heat transfer enhancement.

The unique properties of near-field radiative heat transfer would be very useful in many applications. Near-field heat transfer could allow highly efficient electricity generation from heat [2][11][12]. Also fabrication of novel thermal control devices could be possible [13][14]. It could be possible for example to reach energy conversion with over 30 % efficiency by using near-field heat transfer between a hot thermal emitter and a cold photovoltaic cell [12]. This efficiency is a lot higher than efficiencies reached with the single-junction photovoltaic cells of today. It might be even possible to fabricate thermal transistors by using surface polaritons [14]. All these kind of applications rely on near-field radiative heat transfer between structures.

So far the experiments that have been done have used either spacers or some sort of nanopositioning systems to create the required gap size in three dimensional systems such as parallel plate or sphere-plane systems [4]. Also simpler beam systems have been used in some experiments [5]. The three dimensional systems should provide more interesting results because of the effects which the geometry has on the amount of heat transfer. With 3D systems, one can also achieve large surface areas making the heat transfer stronger and easier to detect. Since the amount of heat transfer scales inversely with the distance, the strongest transfer is reached by having as many points as possible as close to each other as possible. This is why the geometry of two parallel plates is perhaps the best geometry for studying this phenomenon. In addition, the theory is well understood [2][15][16]. The goal of this study was to fabricate a parallel plate geometry by using neither spacers nor nanopositioning systems.

The structure fabrication in this study was done with 3D-lithography which is also known as two-photon lithography [17]. With this method a small gap can be done just by fabricating two structures close together. This method has the advantage that almost any geometry can be fabricated. To create the wanted parallel plate geometry, two cuboid structures were fabricated close together so that there were two parallel walls close to-

gether. This fabrication technique should be accurate enough to fabricate a gap that is in the nanometre scale, because it has been shown that even a 100 nm resolution can be achieved with the 3D-lithography [18]. However, as my earlier experiments in which I studied the fabrication of the basic geometry have shown, there are some issues with getting a small enough gap, because the smallest gap reached with a full size structure was (2.2 ± 0.2) µm [19][20].

Since I had already studied the fabrication of the basic geometry, this study focuses on the later stages of the fabrication. These later stages include mainly the fabrication of the wiring on the two fabricated cuboids. To my knowledge, this kind of two-step fabrication with the 3D-lithography had never been done before, which made this experiment very interesting. Also the novel fabrication technique of ion beam milling [21] was used to find out if a smaller gap size could be achieved with it. The fabricated electronics are basically a resistive thermometer/heater which is basically just a thin metal wire fabricated on both of the two cuboids. This kind of simple resistive electronics were used instead of the more common superconductor-normal metal junctions used in our group [22], so that the heat transfer measurements could be done also at room temperature and even higher temperatures. These fabricated structures were then studied with resistance measurements at different temperatures to show if they could work as a thermometer and a heater.

2 THEORETICAL BACKGROUND

2.1 Near-field heat transfer

The system that is studied in this project is two bodies with parallel walls separated by a small distance in vacuum. This kind of system is represented in Figure 1 by two opaque semi-infinite bodies separated by a distance d. In a system like this the near-field region is reached when the distance d is smaller than the wavelength of the heat radiation and therefore below 1 µm scale for room temperature radiation. In this region, the radiative heat transfer can be several orders of magnitude larger than the classical radiative heat transfer. This can be shown by comparing a classical calculation to a nearfield calculation for the radiative heat transfer.

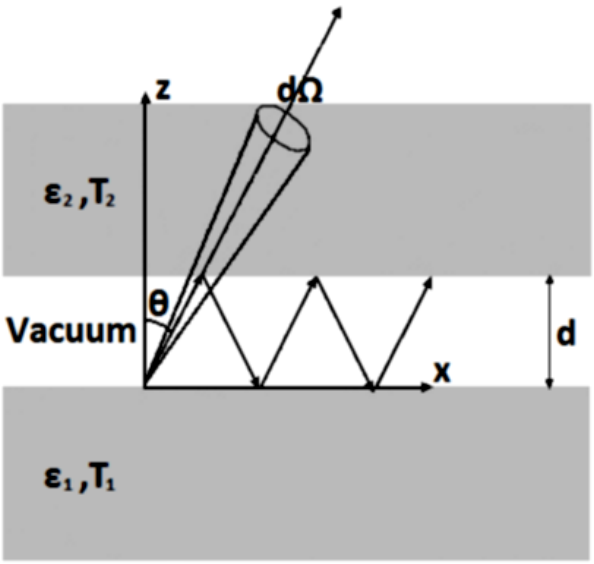

Figure 1: The studied system. There are two semi-infinite media which are at different temperatures and separated in vacuum by a distance d. The arrows represent the multiply reflected rays issued from a ray pointing in the angle $d\Omega$. These multiply reflected rays form the energy transfer in a solid angle $d\Omega$.[15]

Classically the radiative heat transfer is calculated from the energy fluxes coming from the two media. The heat transfer comes directly by calculating the heat flux from the first medium to the second and then subtracting the heat flux from the second medium to the first. The two media are separated by a vacuum which does not emit or absorb radiation which makes the calculation simpler. The fluxes $\phi_{1\to2}$ and $\phi_{2\to1}$ can be calculated by using a pretty simple ray approach. Because ray optics are now used, wave effects are not considered in this simple calculation. As Figure 1 shows, the elementary energy flux $d\phi_{1\to2}$ from the first to the second medium is a sum of the rays that reflect multiple times

between the media. The elementary flux can be written in the form

$$d\phi_{1\to 2}(\theta) = [\varepsilon'_{1\omega}\varepsilon'_{2\omega} + \varepsilon'_{1\omega}\rho'_{1\omega}\rho'_{2\omega}\varepsilon'_{2\omega} + \varepsilon'_{1\omega}\rho'_{1\omega}\rho'_{2\omega}\rho'_{1\omega}\rho'_{2\omega}\varepsilon'_{2\omega} + \cdots]I^0_\omega(T_1)\cos\theta d\omega d\Omega \quad (1)$$

where $\varepsilon'_{1\omega}$ and $\varepsilon'_{2\omega}$ represent the emissivities of the media and $\rho'_{1\omega}$ and $\rho'_{2\omega}$ represent the corresponding reflectivities. The sum in the equation just sums over all the reflected rays and thus the amount of reflectivities increases in the terms. $I^0_\omega(T_1)$ represents the equilibrium radiation intensity at a temperature of T_1 which can be calculated from

$$I^0_\omega(T_1) = \frac{\hbar\omega^3}{4c^2\pi^3}\frac{1}{\exp(\hbar\omega/k_B T_1) - 1} \quad (2)$$

where $\hbar$ is the Planck constant and k_B is the Boltzmann constant. The energy flux can be expressed as a sum of a geometric series by using equation (1). Doing this the energy flux from the first to the second medium can be written in the from

$$\phi_{1\to 2} = \int_0^{2\pi} d\Omega\cos\theta\int_0^\infty d\omega\frac{\varepsilon'_{1\omega}\varepsilon'_{2\omega}}{1-\rho'_{1\omega}\rho'_{2\omega}}I^0_\omega(T_1). \quad (3)$$

The energy flux from the second to the first medium can be calculated similarly and then the radiative heat flux can be written as

$$\phi_{1\to 2} - \phi_{2\to 1} = \int_0^{2\pi} d\Omega\cos\theta\int_0^\infty d\omega\frac{\varepsilon'_{1\omega}\varepsilon'_{2\omega}}{1-\rho'_{1\omega}\rho'_{2\omega}}[I^0_\omega(T_1) - I^0_\omega(T_2)]. \quad (4)$$

If the integrations in the equation are done it will become the Stefan-Boltzmann law which shows that the flux is proportional to T^4. The temperatures T_1 and T_2 in the equations can be either uniform temperatures of the medium or just surface temperatures because the bodies are opaque. Of course when considering the actual fabricated structures the size can be so small that the whole structures are at the same temperature.[15][16]

This calculation gave us the classical radiative heat exchange which is equation (4) but the problem with this calculation is that it does not take into account the different interference effects. With nonmonochromatic radiation, these effects disappear when the distance d is larger than the coherence length l_{coh} but when the distance is smaller than l_{coh} which is the case here these interference effects need to be considered in the calculation.[15]

In addition to the interference effects, evanescent waves are also not taken into account in the classical calculation. Evanescent wave are waves for which the wave vector component k_z is imaginary. This means that evanescent waves do not propagate in the direction of the heat flow, i.e. in the z direction but they decay exponentially. In the studied system an evanescent wave does not carry energy in the z direction inside the vacuum, except when there is another evanescent wave with an opposite wave vector affecting it. However, in the considered geometry, if the second medium is within the wavelength of the evanescent wave, there are evanescent waves produced by reflections at the second interface, with k-vectors in the opposite direction. This means that the evanescent waves can carry energy over the vacuum gap. Considering this, it is clear that the evanescent waves have an effect

on the heat transfer at small distances. This phenomenon is also called the tunneling of evanescent waves, because of the analogy to quantum mechanical tunneling of particles through a barrier.[15][16]

To take these two additional effects into consideration, a more thorough calculation needs to be made. When making a microscopic calculation one has to start from the mechanism which causes the emission of radiation from thermal objects. When there are thermal fluctuations in a material, fluctuating currents are always induced. The mean value of these fluctuating currents is zero but their correlation function is not zero which also means that the average Poynting vector $\langle \mathbf{S} \rangle$ of the electromagnetic fields is not zero. To find this correlation function, one can for example use the fluctuation dissipation theorem [23]. If one wants to find the radiative flux from the first to the second medium, first the average Poynting vector $\langle \mathbf{S} \rangle = \langle \mathrm{Re}(\mathbf{E} \times \mathbf{H}^*) \rangle$ must be calculated, where $\mathbf{E}$ and $\mathbf{H}$ represent the electric field and the magnetic field. $\mathbf{S}$ has units of W/m^2, which are units of energy flux. The Poynting vector can be calculated anywhere, but in this problem it should be calculated through a plane that is just inside the second medium. The electric and magnetic field amplitudes can be written as

$$\mathbf{E}(\mathbf{r}, \omega) = i\omega\mu_0 \int_V \overline{\overline{\mathbf{G}}}_E(\mathbf{r}, \mathbf{r}', \omega) \cdot \mathbf{j}(\mathbf{r}', \omega) d^3\mathbf{r}' \tag{5}$$

$$\mathbf{H}(\mathbf{r}, \omega) = \int_V \overline{\overline{\mathbf{G}}}_H(\mathbf{r}, \mathbf{r}', \omega) \cdot \mathbf{j}(\mathbf{r}', \omega) d^3\mathbf{r}' \tag{6}$$

where the $\overline{\overline{\mathbf{G}}}_E$ and $\overline{\overline{\mathbf{G}}}_H$ represent the Green dyadics of the corresponding field. Here the fields are written in terms of the the thermal source currents $\mathbf{j}$ in a material. The Green dyadics thus give a relation between the current at a point $\mathbf{r}'$ and the electric and magnetic field at a point $\mathbf{r}$, where V is the volume in which the sources are located. The volume can thus be for example the first medium when calculating the heat transfer from the first to the second medium. If an ensemble average is taken over the Poynting vector it is clear that the ensemble average will be over a spatial correlation function of the fluctuations of the thermal currents, see equations (5) and (6). This ensemble average can be calculated with the fluctuation dissipation theorem, which in the frequency domain gives the expression for an isotropic, local dielectric [16]:

$$\langle j_n(\mathbf{r}, \omega) j_m^*(\mathbf{r}', \omega') \rangle = \frac{2\omega}{\pi} \Theta(\omega, T) \epsilon_0 \mathrm{Im}[\epsilon(\omega)] \delta_{nm} \delta(\mathbf{r} - \mathbf{r}') \delta(\omega - \omega') \tag{7}$$

in which ϵ is the dielectric constant and $\Theta(\omega, T) = \hbar\omega/[\exp(\hbar\omega/k_B T) - 1]$ is the mean thermal energy of an oscillator. Specifically the mean energy of an oscillator that is in thermal equilibrium at the temperature T.[15][16]

Next we need the Green dyadic of the electric field. As discussed earlier, this dyadic relates the electric field in the second medium to a source in the first medium. In this case the dyadic is

$$\overline{\overline{\mathbf{G}}}_E(\mathbf{r}, \mathbf{r}', \omega) = \frac{i}{8\pi^2} \int \frac{1}{\gamma_1} (\hat{s} t_{12}^s \hat{s} + \hat{p}_1 t_{12}^p \hat{p}_2) \exp[i\mathbf{K}(\mathbf{R} - \mathbf{R}')] \exp(iz\gamma_2 - iz'\gamma_1) d^2\mathbf{K} \tag{8}$$

in which $\mathbf{r} = (\mathbf{R}, z)$, is the position vector with an in-plane component $\mathbf{R}$ and out-of-plane component z. $\hat{s} = \hat{\mathbf{K}} \times \hat{z}$ and $\hat{p}_j = (|\mathbf{K}|\hat{z} - \gamma_j \hat{K})/k_j$ are the unit polarization vectors, with $k_j = \sqrt{\epsilon_j}\omega/c$ and $\gamma_j = (k_j^2 - \mathbf{K}^2)^{1/2}$, and both the imaginary and real part of γ_j are defined always positive [24]. The two coefficients t_{12}^s and t_{12}^p denote the amplitude transmission coefficients between the first and the second medium for s and p polarizations. For the planar geometry, these coefficients can be written in the form

$$t_{12}^{s,p} = \frac{t_{13}^{s,p} t_{32}^{s,p} \exp(id\gamma_3)}{1 - r_{31}^{s,p} r_{32}^{s,p} \exp(2id\gamma_3)} \tag{9}$$

where they are expressed in terms of the Fresnel reflection and transmission coefficients r and t between the two materials and vacuum (3) [24] and the distance d. When one knows the Green's function for the electric field $\overline{\overline{\mathbf{G}}}_E$, equation (8), the Green's function for the magnetic field $\overline{\overline{\mathbf{G}}}_H$ can be calculated by using the Maxwell equations [24]. With both the Green functions known, the heat transfer per unit area can be calculated. This quantity is given by $\phi(T_1, T_2) = \langle S(d^+, T_1)\rangle - \langle S(0^-, T_2)\rangle$ and can now be written as

$$\begin{aligned}\phi(T_1, T_2) = \frac{4}{\pi^2} \int_0^\infty d\Omega[\Theta(\omega, T_1) - \Theta(\omega, T_2)] \int_0^\infty K dK |\exp(id\gamma_3)|^2 \\ \times \left[\frac{|\gamma_3|^2}{|1 - r_{31}^s r_{32}^s \exp(2id\gamma_3)|^2} \frac{\mathrm{Re}(\gamma_1)\mathrm{Re}(\gamma_2)}{|(\gamma_1 + \gamma_3)(\gamma_2 + \gamma_3)|^2} \right. \\ \left. + \frac{|\gamma_3|^2 |\epsilon_3|^2}{|1 - r_{31}^p r_{32}^p \exp(2id\gamma_3)|^2} \frac{\mathrm{Re}(\gamma_1^* \epsilon_1)\mathrm{Re}(\gamma_2^* \epsilon_2)}{|(\gamma_1\epsilon_3 + \gamma_3\epsilon_1)(\gamma_2\epsilon_3 + \gamma_3\epsilon_2)|^2} \right],\end{aligned} \tag{10}$$

in which $K = |\mathbf{K}|$. If the K integration was done from 0 to ω/c, only the waves which propagate in the vacuum gap would be taken into consideration. Now that the integration is to infinity, also the contribution of the evanescent waves with $K > \omega/c$ is in consideration. We are now interested in very small distances and the main approximation is the fact that nonlocal electrodynamics are not considered. For metals this approximation should be valid if the used distances are larger than the Fermi wavelength [25]. Typically this is not a problem, because the smallest distances in practise are in the nanometre scale, still far from the Fermi wavelength which is ∼5 Å in good metals. For insulators, non-locality would set in at even smaller atomic distances ∼1 Å.[2][15]

The heat transfer from equation (10) can be simplified further [15][16]. The heat transfer that comes from the dissipation of the fields in the second medium, formed by the currents in the first medium is denoted $\phi_{1\to2}$. The total heat transfer can then be written as the sum of two terms $\phi_{1\to2} = \phi_{1\to2}^{\mathrm{prop}} + \phi_{1\to2}^{\mathrm{evan}}$ which represent the contributions of the propagating and evanescent waves, respectively. Using the angle θ defined in Figure 1, the energy flux in a solid angle $d\omega = 2\pi c^2 K dK/(\omega^2 \cos\theta)$ coming from the propagating waves can be written in the from

$$\begin{aligned}\phi_{1\to2}^{\mathrm{prop}} = \int \frac{d\Omega d\omega \cos\theta}{2} I_\omega^0(T_1) \\ \times \left[\frac{(1 - |r_{31}^s|^2)(1 - |r_{32}^s|^2)}{|1 - r_{31}^s r_{32}^s \exp(2id\gamma_3)|^2} + \frac{(1 - |r_{31}^p|^2)(1 - |r_{32}^p|^2)}{|1 - r_{31}^p r_{32}^p \exp(2id\gamma_3)|^2} \right].\end{aligned} \tag{11}$$

where the coefficients $r_{31}^{s,p}$ and $r_{32}^{s,p}$ are the reflection coefficients between the vacuum and the first medium, and between the vacuum and the second medium for the s and p polarizations. Since the coefficients r are reflection coefficients, the expressions $1-|r|^2$ give the transmissivity, and these transmissivities can be identified as emissivities. As we see, this equation is very similar to the earlier equation (3). The different looking denominator in this equation comes from the fact that equation (11) takes interference into account. Equation (11) actually reduces to equation (3) after two simple steps. If the reflection coefficients evolve slower with frequency than the expression $\exp(i\gamma_3 d)$, we can take the mean average of $1/|1-r_{31}r_{32}\exp(2i\gamma_3 d)|^2$, giving $1/(1-|r_{31}|^2|r_{32}|^2)$, getting equation (3).[15][16]

For $\phi_{1\to 2}^{\text{evan}}$, we cannot define the directional emissivity, because the evanescent waves are propagating along the interface with no real k_z component. The surface waves are characterized by their in-plane wave vectors $\mathbf{K}$, however, and thus an emissivity as a function of $\mathbf{K}$ can be defined. Doing this one gets the expression for the contribution of the evanescent waves

$$\begin{aligned}\phi_{1\to 2}^{\text{evan}} = &\int_0^\infty d\omega I_\omega^0(T_1)\frac{c^2}{\omega^2}\int_{\omega/c}^\infty 2KdK\exp[-2d\text{Im}(\gamma_3)] \\ &\times\left[\frac{\text{Im}(r_{31}^s)\text{Im}(r_{32}^s)}{|1-r_{31}^s r_{32}^s\exp[-2d\text{Im}(\gamma_3)]|^2}+\frac{\text{Im}(r_{31}^p)\text{Im}(r_{32}^p)}{|1-r_{31}^p r_{32}^p\exp[-2d\text{Im}(\gamma_3)]|^2}\right].\end{aligned} \tag{12}$$

If this equation is compared with equation (3) it must be noted that the expressions $\text{Im}(r_{31}^{s,p})$ and $\text{Im}(r_{32}^{s,p})$ can be identified as generalized emissivities for the first and the second medium, respectively. After this is done, the equations start to look very similar. Now there is the additional term $\exp[-2\text{Im}(\gamma_3)d]$ which just adds an exponential decay, which accounts for the decay of the evanescent waves with z. This result shows that if the distance between the two media is small enough to allow interactions between the decaying surface waves, there is an energy transfer which can be called the tunneling of evanescent waves.[2][15][16]

Using the expression for heat transfer from equation (10), the radiative heat transfer coefficient h^R can be written as

$$h^R(\omega) = \lim_{T_1\to T_2}\frac{\phi(T_1,T_2)}{T_1-T_2}.[26], \tag{13}$$

having units W/(Km^2) i.e. conductance per unit area. As an example this transfer coefficient $h^R(\omega)$ is drawn in Figure 2A as a function of the distance d for two different polar media, glass and SiC, at room temperature. In the figure it is easy to spot the classical and the near-field regions. Because the coefficient does not depend on the distance when the distance is larger than 10 µm, that is the classical region, where transfer happens only due to propagating waves. When the distance becomes smaller than 10 µm, the transfer starts increasing as $1/d^2$. This is the near-field region. In Figure 2B there is the spectral dependence of the heat transfer coefficient when the distance is 10 nm. The figure shows that only certain frequencies which correspond to resonant surface waves (photon polaritons) are important for the transfer. It can thus be said that heat transfer

is practically monochromatic in the near-field region. In the monochromatic limit, the heat transfer coefficient can be asymptotically expanded for short distances, in this case giving the expression

$$h^R(\omega) = \frac{1}{d^2\pi^2}\frac{\mathrm{Im}(\epsilon_1)\mathrm{Im}(\epsilon_2)}{|1+\epsilon_1|^2|1+\epsilon_2|^2}k_B\Big(\frac{\hbar\omega}{k_BT}\Big)^2\frac{\exp[\hbar\omega/(k_BT)]}{(\exp[\hbar\omega/(k_BT)]-1)^2}. \tag{14}$$

From this equation the $1/d^2$ relation which was mentioned earlier can be directly seen. In addition, the strong dependency on frequency is apparent from this expression, remembering that ϵ is also frequency dependent [2]. There is a peak in the transfer coefficient when the dielectric constant approaches -1, which tells us that the transfer is caused by surface waves. Because the thermal resistance over a vacuum gap of 10 nm is much larger than the resistance over about 100 nm in solid material, the temperature will be uniform over a skin depth in the medium, and the calculation should be valid for the studied system. Now it has been shown that the heat transfer in the near-field can be orders of magnitude larger than the classical heat transfer.[15][16]

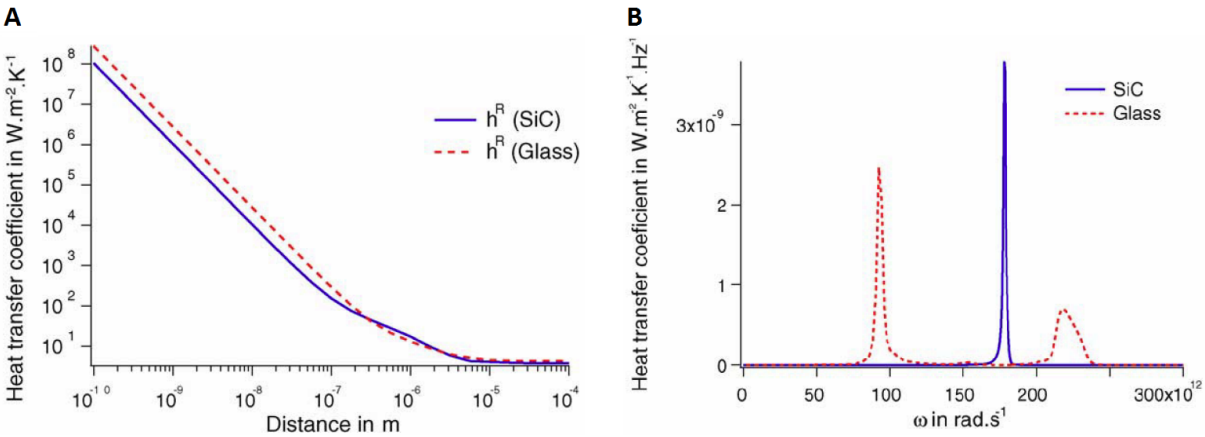

Figure 2: A, the radiative heat transfer coefficient h^R as a function of the distance d between two for semi-infinite media, SiC-SiC or glass-glass, at a temperature of 300 K. B, the spectral heat transfer coefficient at a temperature of 300 K when the distance d is 10 nm.[15][16]

2.2 Review of previous near field experimental set-ups

There have been many different geometries that have been used for near-field measurements by different groups. The different geometries include tip-plane, sphere-plane, parallel beam and parallel plate geometries. Figure 3 shows the theoretical near-field heat transfer as a function of the gap size for the different geometries. If one was to add the tip-plane geometry to the figure, it would be even lower than the sphere-plane curve. This tip-plane geometry has been studied for example by K. Kim et al. (2015) [6] with a scanning thermal microscope. This is the easiest geometry to fabricate because the tip of the microscope works as the tip, and only a plate has to be fabricated. This is why this geometry was the first that was used for measurements. The tip-plane geometry is very similar to the sphere-plane geometry that has been studied recently by B. Song et al. (2015) [7] and K. F. Chen et al. (2015) [8]. The sphere-plane set-ups have actually given the largest subwavelength enhancements, but this geometry like the tip-plane geometry

allows near-field heat transfer only at the tip of the sphere. Because the transfer happens only at the very tip, the total heat current is very small. Also the smallest gap achieved with sphere-plane geometry was around 400 nm.

The first plane-plane geometry set-ups were fabricated using spacers with low thermal conduction [9]. These spacers were needed to have good parallelism between the plates. However due to these spacers, the enhancement was a lot lower than the theoretically predicted value. The latest studies have used different custom built nanopositioning systems to produce parallel beam [5] and parallel plate [10] geometries without spacers. For the parallel beams, the positioning system was a micromechanical platform activated by electrostatic forces, and for the plates a nanopositioning platform with piezoelectronics. The beams used for the measurements were monolithic beams of SiC measuring 0.3 µm by 155 µm. The parallel plates were fabricated by coating parallel surfaces (48 µm x 48 µm) with SiO_2 or Au. The positioning systems are hard to make, and thus only very recently it has been possible to fabricate these geometries with good enough parallelism.

The curves in Figure 3 all have a $1/d^{\alpha}$ dependence when the gap is smaller than 200 nm which is called the deep subwavelength regime. The geometry-dependent factor α can be determined by fitting the experimental data. With the parallel-beam geometry, an α of 1.54 [5] was achieved. This is only a bit higher than the theoretical value for cylinder-cylinder geometry ($\alpha = 1.5$). With the parallel plate geometry, the value for α was 1.8 [10]. Considering that the value predicted by theory is 2.0, this indicates very good parallelization. However neither of these two setups can reach gap sizes below 20 nm, and because the positioning systems occupy a large area, the total radiative heat current per area is low. So there is still a lot of room for improvement before these geometries can be used for actual applications. It is clear that the parallel plate geometry should have the highest total heat transfer which is why this geometry was chosen for this study. Now the plan was to create this geometry without the complicated nanopositioning systems by already fabricating the parallel plates close together.

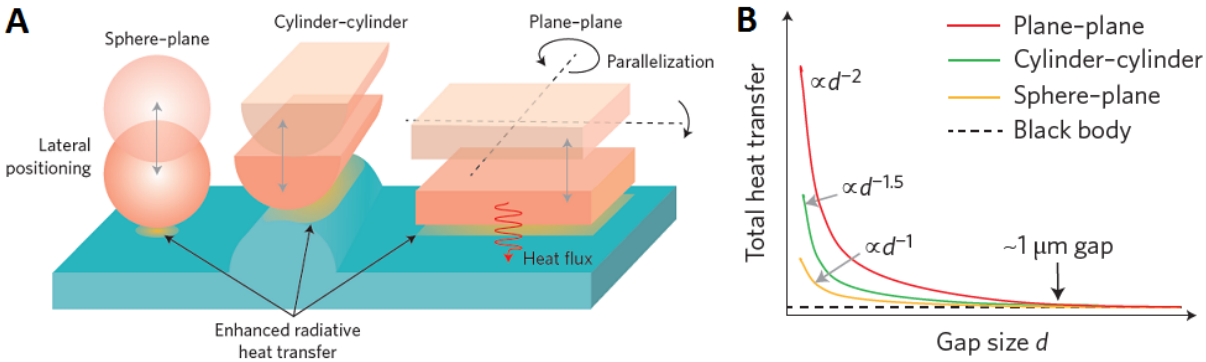

Figure 3: A, Schematic diagram of the different geometries for enhancement of radiative heat transfer. B, The gap-size dependence of total heat transfer for different geometries. The plane-plane geometry has the highest enhancement with the largest geometry-dependent factor α in the deep subwavelength regime.[4]

2.3 Fabrication methods

2.3.1 3D-lithography

3D-lithography is a technique in which a resist can be exposed one three dimensionally isolated point at a time. These isolated points are called voxels. This kind of process can be done with laser lithography, which takes advantage of two-photon absorption [27]. Because of the use of two-photon absorption, 3D lithography is often called two-photon lithography. To be able to expose only one voxel at a time, the laser needs to be focused accurately to a point where this two-photon absorption then happens. The used resist and laser wavelength have to be such that the resist can be only exposed by the absorption of two photons at the same time, and not by just one photon. To fabricate a structure, either the beam or the resist has to be moved so that the focal point of the laser draws the wanted structure in to the resist.

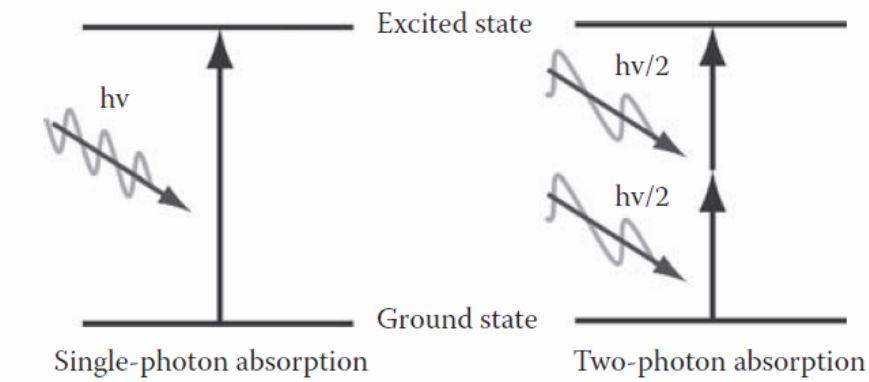

Figure 4: Comparison between one- and two-photon absorption in an energy diagram. In the figure h represents the Planck constant and v represents the frequency of the radiation.[28]

In two-photon absorption a material absorbs two photons at the same time instead of just one which is the usual case. When the material absorbs these two photons it goes from its ground state to an exited state which has an energy equal to the sum of the two absorbed photons. The difference between one- and two-photon absorption is depicted in Figure 4 as a simple diagram. Because the two photons can't always absorb at the same exact time a virtual state can also be used to explain the process. It can be thought that the first photon excites the material to a virtual state, and then the second photon which absorbs within a femtosecond then excites the material to the actual exited state [17]. The two photons which are absorbed can thus have a different energy as long as the sum of the energy is enough to excite the material. Usually only one wavelength is used in practice, as lasers are required for high intensity.

Normal single photon absorption is a linear process but two-photon absorption depends on the square of the intensity of the radiation, which means that it is a nonlinear process. This process can be described by a simple expression, which shows the change in intensity over a distance dz. The expression can be written in the form

$$\frac{dI}{dz} = \alpha I + \beta I^2, \tag{15}$$

where α is the absorption coefficient for single photons, β is the two-photon absorption coefficient and I is the intensity of the radiation [29]. The two-photon absorption coefficient β is dependent on the medium. It is linearly proportional to the imaginary part of the third-order nonlinear susceptibility $\chi^{(3)}$ for the two-photon absorption process [27]. Equation (15) thus shows that two-photon absorption is only relevant at high intensities.

Two-photon absorption can be used to expose resists specifically designed for it, but also most normal UV resists. The frequency has to be set so that it is about half of the frequency of the UV radiation, making it infrared radiation. When this is the case, the energy of two infrared photons will have the same energy as one UV photon, as was shown in Figure 4. Because the two-photon absorption is nonlinear, it only happens in the spot where the light is well focused to high intensity, and thus a resist can be exposed only in a small 3D-spot called a voxel [30]. If the resist was exposed with linear one-photon absorption, the polymerization would happen in a lot larger area, or even everywhere in the path of the radiation. This difference can be nicely seen in Figure 5 where the volumes in which the different absorptions take place are compared. This is the reason why three-dimensional lithography is possible with two-photon absorption. To be able to do two-photon lithography in practise, one needs to reach the required radiation intensity. This can be done with a femtosecond pulsed laser which is focused with a microscope objective, as is done for example in the Nanoscribe Photonic Professional system used in this project.

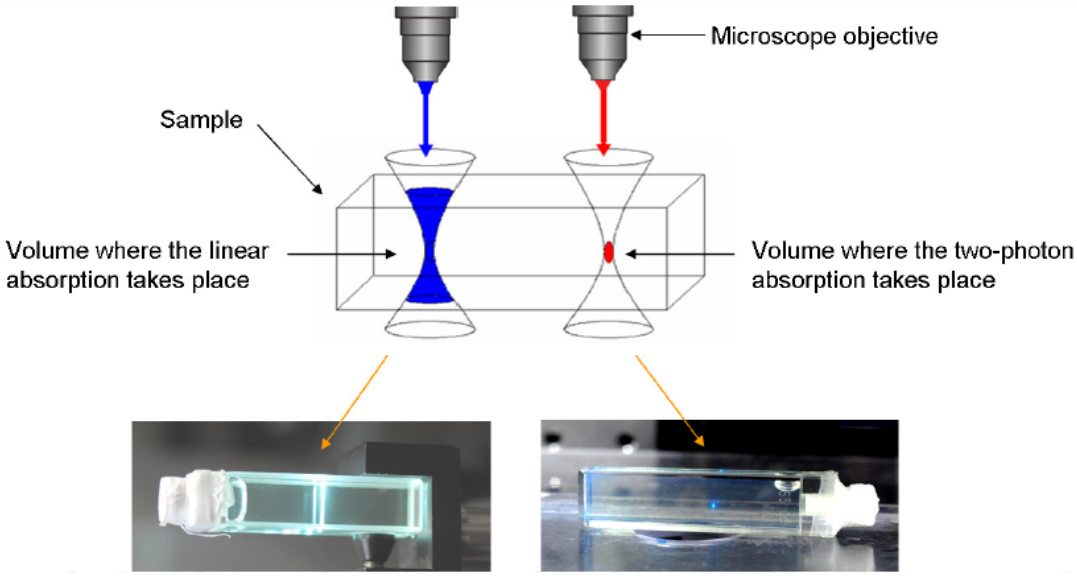

Figure 5: The difference between linear and two-photon absorption. With linear absorption, the whole volume crossed by the beam is excited, but with two-photon absorption only a small volume or voxel around the focal point is excited. The blue light in the two photographs is due to fluorescence in the excited part of the sample.[31]

2.3.2 Atomic layer deposition

Atomic layer deposition (ALD) is a film deposition technique which is based on sequential use of reactions. These reactions need to be self-limiting and also they have to be gas-solid reactions. A schematic of these sequential self-limiting reactions is shown in Figure 6. Basically, ALD is a chemical vapor deposition (CVD) technique used for inorganic film deposition. Thanks to the self-limiting factor of the reactions used, it can produce films that are even a fraction of a monolayer thick. ALD can also be used to coat samples with very complex shapes conformally, because the self-limiting reactions take place everywhere on the surface of the sample. Since gas-solid reactions are used in ALD, the precursors are always in gas phase and these gasses are only introduced to the sample chamber sequentially, so that there are no gas phase reactions between the precursors. If these gas phase reactions could happen, the formation of granular films would be possible. The reaction cycles used in ALD are often binary reaction sequences where just two reactions occur and fabricate a binary compound film on the surface of the sample. The reactions are self-limiting because there are only a finite number of surface sites where the reactions can happen.[32][33]

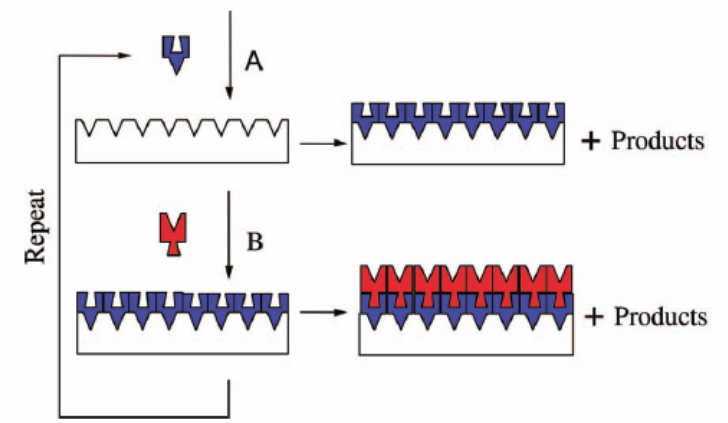

Figure 6: A representation of a sequential self-limiting AB reaction cycle used in ALD.[34]

The process which is often used as a model for this technique is the ALD growth of Al_2O_3 which was also the process used in this study. The surface chemistry happening in this process can be described as

$$(A)\ Al_2OH^* + Al(CH_3)_3 \longrightarrow AlOAl(CH_3)_2{}^* + CH_4 \tag{16}$$

$$(B)\ AlCH_3{}^* + H_2O \longrightarrow AlOH^* + CH_4 \tag{17}$$

where the asterisks are used to denote surface species. The aluminium oxide grows during alternating exposures to trimethylaluminum (TMA) and H_2O. This process is represented graphically in Figure 7. The reason why this is used as a model system is the fact that the reactions used are very efficient and self-limiting. The main reason for the efficiency is the formation of a really strong Al−O bond. The reactions can be combined to an overall reaction which is

$$2\,Al(CH_3)_3 + 3\,H_2O \longrightarrow Al_2O_3 + 3\,CH_4,\ \Delta H = -376\text{kcal}. \tag{18}$$

As can be seen the reaction enthalpy is negative and very high for this reaction, which means that the reaction releases a lot of energy. This enthalpy is actually one of the highest that have been encountered for any reaction used in ALD.[33]

The aluminum oxide ALD reactions have also been modeled with density functional theory (DFT) [35]. The calculations showed that $Al(CH_3)_3$ is complexed to $AlOH^*$ species prior to its surface reaction which causes it to be in a deep precursor well before the reaction. The calculations also showed that H_2O is in a similar well because it complexes to $AlCH_3{}^*$ species before its surface reaction. The formation of these complexes is due to very strong Lewis acid-base interactions. The formation of these complexes between the precursors and the active sites on the surface is also called the adsorbed state. The complexes form between the empty p orbitals of the Al atom and lone pair electrons of oxygen. The formation of these stable complexes on the surface makes the surface reactions very efficient.[33][35]

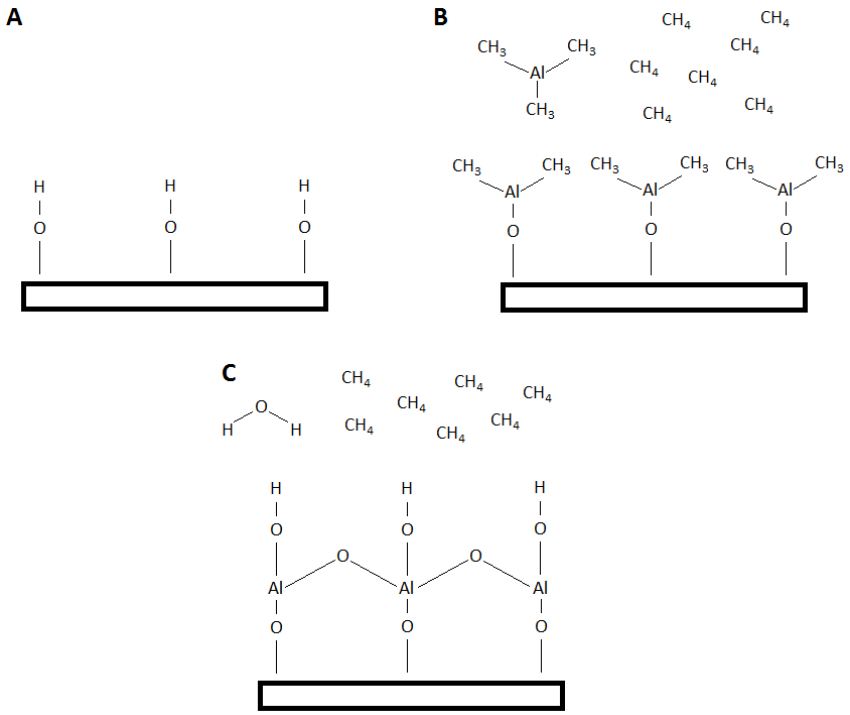

Figure 7: A representation of the Al_2O_3 ALD surface reactions. A, the hydroxyl groups which are on the sample surface before any precursor is introduced. B, when TMA is introduced it binds to the hydroxyl groups which are on the surface. C, after introducing the second precursor which is water vapor, the H_2O molecules react with the dimethyl aluminium surface species forming oxygen bridges and new hydroxyl surface species. In both the phases B and C methane is released.[36]

2.3.3 Helium ion microscopy and milling

Helium ion microscopes (HIM) are very similar to scanning electron microscopes (SEM). In both techniques the surface of a sample is scanned with particles and then the emitted secondary electrons are detected. The difference is that the particles used in SEM are negative electrons and in HIM they are positive ions. For imaging, the ions are normally helium ions. Other ions that can be used are neon and gallium ions. The quantity that is actually measured in both HIM and SEM is the secondary electron intensity, which is detected usually with an Everhart-Thornley (ET) detector. This secondary electron intensity from the different raster scanned spots on the sample is then used to form the image. The resolution of a HIM can be around 0.3 nm, which is better than the 0.5 nm resolution that can be achieved with the best SEMs. Other advantages of the HIM are its better depth of field and the possibility to image nonconductive samples. Nonconductive samples can be imaged with a HIM by using an electron flood gun to neutralize the positive charging caused by the ion beam. This kind of electron flood gun is used for example in the Zeiss Orion Nanofab system used in this study. Helium ion microscopes can also be used for ion beam milling, but depending on the material, heavier ions like neon ions might have to be used. This is why the system used in this study has the option to use neon gas when milling. The milling is exactly the same process as imaging and thus a small amount of milling happens always when a sample is imaged. The difference between imaging and milling is basically just the used beam current. For milling a large current is used to increase the sputtering rate.[21]

In HIMs the ions are produced with a gas field ion source (GFIS). In the Orion Nanofab this source is a very sharp tungsten tip. Then, by using the microscope itself, the tip is sharpened by removing atoms from the tip by using a very high voltage. Atoms are removed until there is only a trimer at the end of the tip. This means that only three tungsten atoms work as the ion source. The ions are then formed only at this very sharp tip, because of the high ionization energy of helium and due to the electric field being strongest at the very tip. Helium is the gas of choice for imaging, because it has the highest ionization energy of any gas. The reason why the tip is sharpened until there is a trimer left and not until there are two atoms or a single atom is because a trimer is very stable. Each of the three atoms in the trimer emits ions in a Gaussian angular distribution. These emission cones leaving the tip have an angular separation of about 1°. Only one of these three beams is aligned with the beam defining aperture.[21]

In Figure 8, there is a schematic of a HIM column and the beam, after the alignment through the aperture is made. As shown in the figure the quadrupole deflectors are used for the beam alignment. The zoom lens is used to focus an image of the source into a beam crossover above the aperture. The SFIM (scanning field ion microscopy) imaging mode is the mode used for the imaging of the source when the trimer is built. The selective aperture is used to choose the amount of the emitted beam that is used for the imaging. Changing the aperture is the main way to change the beam current. The octopole deflectors are used for the scanning in the normal imaging mode. Finally, the objective lens focuses the beam to the sample. The column is very similar to a SEM column. The only difference is that instead of the magnetic lenses used in SEMs, the whole column is completely electrostatic in HIMs. This is because only electrostatic lenses can have appropriately short focal lengths for ions at the needed acceleration voltages of about 30 kV.[21]

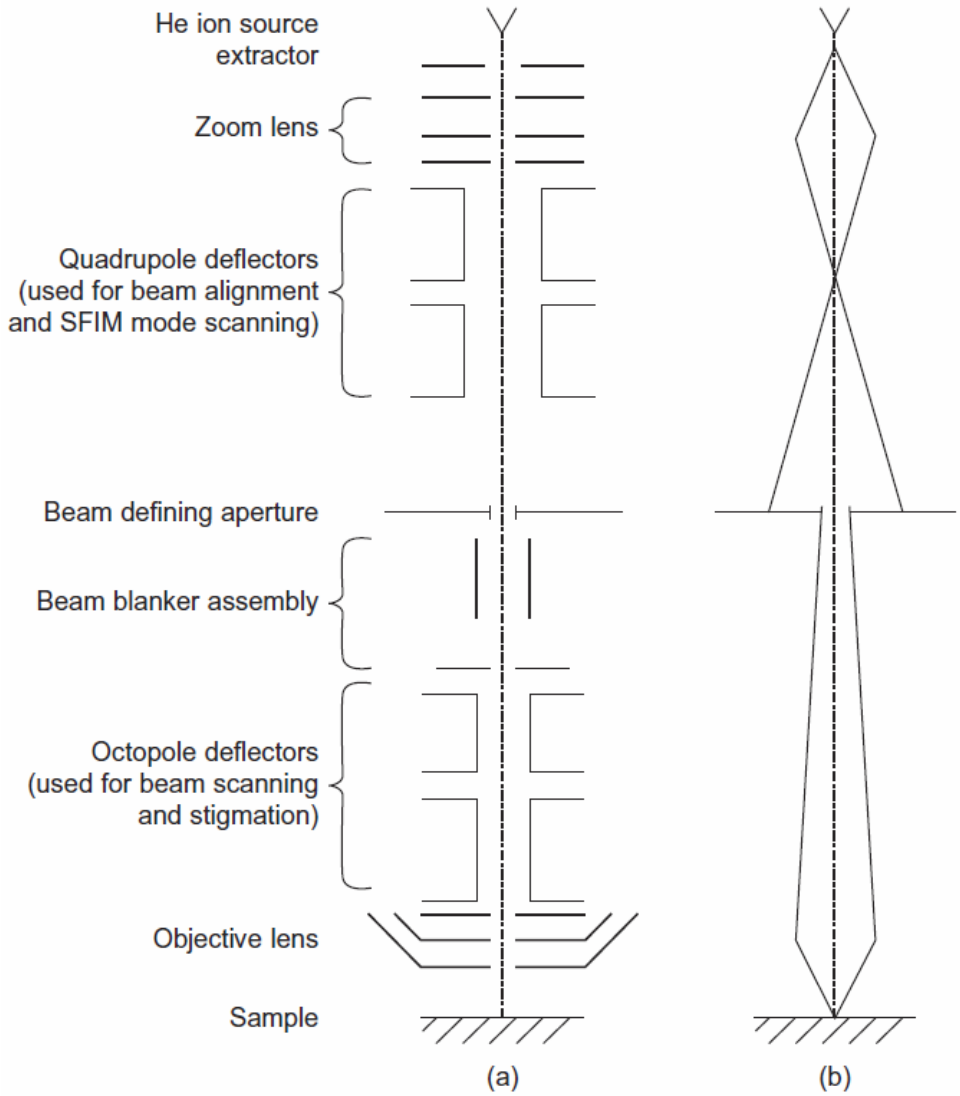

Figure 8: A simple schematic of a HIM column. (a) The different components of the column. (b) The beam in normal imaging mode.[21]

2.3.4 Physical vapor deposition

PVD (physical vapor deposition) usually means the ejection of material from a solid target material. The ejected material is then transported in a vacuum to a substrate surface, and this causes film deposition to happen on the surface. There are a lot of different ways to eject atoms from a target material. Two different techniques were used in this study, which are heating and ion bombardment. The first of these techniques is called evaporation and the other is sputtering. Evaporation is in theory a very simple technique. Metals can be evaporated just by heating, because hot metals have a high vapor pressure. When a hot metal is put in vacuum, the evaporated atoms will transport to a sample. The systems used for evaporation are either UHV (ultrahigh vacuum) or HV (high vacuum) systems. The evaporator used in this study was a UHV system which means that it can achieve a very good film quality. When the vacuum is good enough, the metal atoms will not experience any collisions. The reason why there are no collisions is that the MFP (mean free path) is larger than the size of the evaporation chamber. Since there are no collisions, the atoms take a line-of-sight route to the sample. Because of the line-of-sight

transport and low deposition temperature, the film quality is best on planar surfaces and no coating happens on the sidewalls of structures. This is why in evaporation the samples usually need to be coated from multiple angles. In evaporation, the heating of the metal can be done in various ways. One way is electron beam evaporation which is depicted in Figure 9A. This is the heating method in the UHV instrument used in this study.[37]

In sputtering, the atoms of a negatively biased target are ejected by positive argon ions coming from a glow discharge plasma. Similarly to evaporation, the ejected atoms are then transported in a vacuum to the substrate. In sputtering these atoms hit the substrate with a high energy which improves adhesion, because the energetic atoms knock out loosely bound impurity atoms from the surface. If the energies are too high, the sample can be damaged, however. In sputtering, the deposition rates are typically higher than in evaporation. Also because the pressures used for sputtering are quite high, the ejected atoms experience a lot of collisions while transporting to the sample. So in sputtering the transport is not line-of-sight and thus sidewalls of structures will also be coated, and multiple angles don't have to be used. There is a simple depiction of sputtering in Figure 9B.[37]

The deposition thicknesses are usually monitored with a QCM (quartz crystal microbalance). A QCM can monitor the change of a mass by measuring the vibration frequency of a single crystal quartz resonator. The measured resonant vibration frequency is very precisely measurable, and dependent on the mass of the system. The frequency can be measured via the piezoelectric effect. When material is deposited on the crystal, the mass of the system changes and thus a QCM can also be used to measure the thickness of the deposition. The precision of a QCM can be so good that it can detect the difference of one or a few atomic layers. A QCM is used for example in the UHV evaporator used in this study.

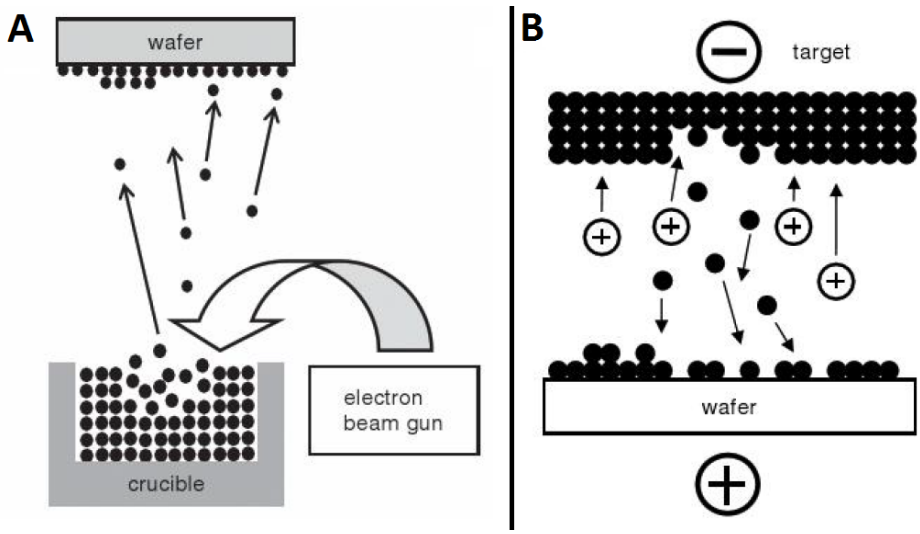

Figure 9: A, evaporation with an electron beam. The metal is heated with an electron beam that is directed with a magnetic field which causes the metal to vaporize. The evaporated atoms are then transported in vacuum to the substrate. B, ion sputtering. Ions formed in the plasma eject atoms from the target and the ejected atoms are transported in vacuum to the substrate.[37]

3 MATERIALS AND METHODS

This study was mostly done by fabricating multiple different structures using various nanofabrication methods, and then analyzing the structures using different imaging methods. More or less the same process was used for all structures, but the structures were studied in different phases of the process, and also different possibilities were studied for the different fabrication steps. Taking into account all the fabrication steps, the fabrication of one sample took three days. The fabrication takes a long time because of the very long lithography and ALD steps. In addition to just studying the structures by imaging, measurements were also done on the structures. They were resistance measurements, done to find out if the fabricated electronics could work as a heater and a thermometer. For the resistance measurements, two different setups were used.

3.1 Sample fabrication

3.1.1 Design

When fabricating structures with 3D-lithography using a Nanoscribe Photonic Professional, first a design has to be made for the structure. For samples in this study both a three dimensional base structure and a wiring were needed, both designed with Matlab. The Describe software, which normally decodes the designs and converts them to machine instructions for the Photonic Professional also allows the use of 3D CAD software such as Inventor, but Matlab allows for more accuracy with the design, especially with larger 3D structures. The better accuracy comes mostly from the fact that Matlab allows the accurate design of the interior of the structure also, whereas the Describe software can only do certain types of hatching for the interior. In other words, with 3D CAD programs one can only design the overall shape of the structure. With Matlab, the designing was done by first writing a code for which one can give the wanted parameters, such as the scan mode and laser power. This code then creates a point group, which contains the start point and end point of every line that has to be drawn to fabricate the structure. Using this point group, the Photonic Professional can then fabricate the structure. The point group and the parameters have to be given to the Photonic Professional as a GWL file, so the Matlab code was set to output such a file. The Matlab code was written by me with the help of Geng Zhuoran.

For the base structures the used Nanoscribe lithography parameters were always the same, listed in Table 1. The laser power is selected as a percentage of the maximum 20 mW, and thus only the percentage value is given to the machine. The designs for the wiring were done similarly to the designs for the base structures, but the parameters had to be changed. Perfect shape could not be used due to too high speeds, and thus had to be set to off. Then different speeds were used in the test by using different update rates and point distances. The Describe software was always used to inspect the used GWL files before doing the actual lithography. This is easily done with the Describe, because with the program, one can see how the structure will be drawn step by step, and also the time needed for the lithography can be seen. Figure 10 shows what a designed base structure

of one block looks like in the Describe program. Two such blocks will be drawn near each other for the near field experiment.

Table 1: The Nanoscribe lithography parameters for the base structures.

Parameter	**Value**	**Parameter**	**Value**
Scan mode	Piezo scan	Measure tilt	3
Continuous mode	On	Invert Z-axis	1
Connect points	On	Find interface at	0.2 µm
Perfect shape	Intermediate	Laser power	40 %
Time stamp	On	Power scaling	1
Tilt correction	On	Settling time	200 ms

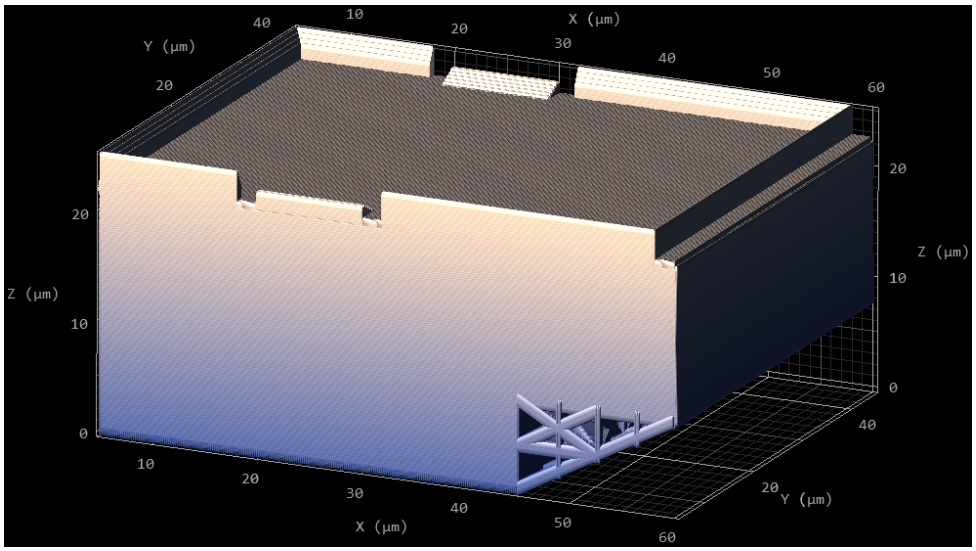

Figure 10: A model of a structure made with the Describe program.

3.1.2 Lithography for the base structures

The Nanoscribe Photonic professional system used for lithography uses two-photon absorption to create three dimensional structures. The system is controlled with a computer and it uses piezoelectronics to accurately move the sample stage. A photograph of the system is shown in Figure 12A. For the base structures, the DiLL (Dip in Laser Lithography) method of the Photonic Professional system had to be used, because the substrates used in the fabrication were sapphire and not glass for which the DLW (Direct Laser Writing) method is designed. The DiLL method also has the advantage of not having to draw through already drawn layers, because the laser comes from the top and not through the substrate as is the case with the DLW method. This is an advantage because it allows the use of the same laser power for the entire structure. With DLW the laser power has to change with high structures. The difference between DLW and DiLL methods is shown in Figure 11. Because the DiLL method was used, the illumination had to be set to RI (reflection illumination) and the objective had to be the EC PLNN 100x/1.3 Oil objective. The size of the sapphire substrates used for the samples was 8 mm x 8 mm. This size was too small for the sample stage in the Photonic Professional, and thus those chips had to be first glued on glass substrates which were then glued onto the sample stage. Because the DiLL method was used for the lithography, IP-Dip resist designed for the DiLL method

had to be used. Another thing to remember with the DiLL method is that the z-axis in the software has to be inverted because the laser does not go through the substrate. With the base structures, the perfect shape function which basically finds the optimal movements for the stage was always used. This meant that an extra calibration for the perfect shape had to be done before each exposure. This calibration is done through the Nanowrite software, which controls the system, and it can be found under perfect shape settings. After the exposure was done, the samples were developed in PGMEA (propylene glycol monomethyl ether acetate). The development time was 20 minutes for all samples. This time was optimized in earlier experiments [19]. After the development, the samples were cleaned with IPA (isopropanol) and then dried with nitrogen gas. Because the IP-Dip is a negative resist, the PGMEA removes all the resist that has not been exposed, leaving only the drawn structures on the substrate.

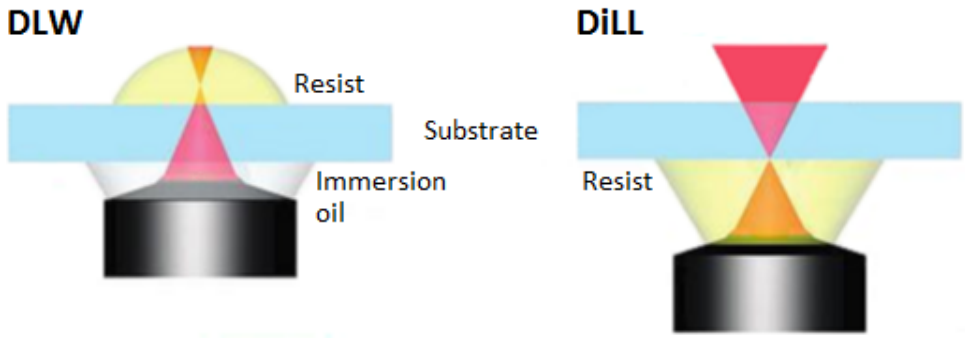

Figure 11: The difference between the two patterning modes. DLW can only be used with a transparent substrate, but DiLL works on any substrate.[38]

3.1.3 Coating the base structures with aluminium oxide

After the base structures were fabricated, they were coated with Al_2O_3 using ALD. This is done to make the structures stronger so they can survive the later fabrication steps, and also to provide a known material on the structures so that the heat transport could be more easily characterized. The reason for using Al_2O_3 was the fact that it is a strong material and its characteristics are well known. Also the ALD process for Al_2O_3 is very simple. Even though this step is pretty important, it was not done for all the samples because it is very time consuming. This step was only done to the later samples which were going to be used for the resistance measurements. For the earlier fabrication experiments, it would not have been efficient to have this step in the process. The ALD was done using a Beneq TFS 200 system, which is shown in Figure 12B. The wanted thickness for the Al_2O_3 film was 50 nm so that it makes the structure a bit stronger but does not take too much time. The cycle used for the deposition was first 500 ms of TMA, then a 5 s purge, then 500 ms of H_2O and, then a 10 s purge. The temperature used in the ALD was 50 °C. With this recipe the growth had been determined in earlier experiments to be 0.1 nm per cycle [20]. This meant that the amount of cycles needed was 500, so that the total depostion time was 2 h 13 min.

3.1.4 Coating the base structures with a resist

The main way of coating the samples with photoresist was spinning. The spinner used for this was a Bidtec SP-100 and the resist was AR-P 3120. The spinning was done in 800 nm layers. To get a layer of 800 nm, the samples were spun at 1500 RPM for 90 seconds. Usually the time used for spinning is 60 seconds, but I quickly found out that when using the small 8 mm x 8 mm substrates there was easily extra resist on the edges of the substrate. This problem was solved by spinning the samples for a longer time. To get thicker films of resist, multiple layers were used but the parameters for the spinning were always the same. After the spinning and also between the multiple layers, the samples were baked in 100 °C. Normally the baking was done for 1 minute, but when doing baking between layers the time was shortened to 30 seconds. For the first fabrication experiments, only one layer of resist was used, but when coating 3D structures it quickly became clear that more layers were needed. After testing, four layers was found to be a good amount. So for all the later samples four 800 nm layers of resist were used.

The other coating technique tested in this study was dip coating. For this, a modified Langmuir-Blodgett thin film coating device by KSV instruments was used. The dipping was only done directly vertically at a dipping speed of 10 mm/min. This was actually pretty much the highest speed setting, with which the speed stayed constant. This high speed was used to get a layer that was as thick as possible. There had been no dip coating experiments done with this AR-P resist but I found results with other solutions which had very similar viscosity. These results stated that with a speed of 10 mm/min the thickness would be around 160 nm [39]. To get thicknesses of around a micrometre, the speed would have to be an order of magnitude higher which was impossible to achieve with this setup.

3.1.5 Lithography for the wiring

Normally when wiring is fabricated, electron beam lithography is used because of its high resolution. However, now the lithography had to be done on top of 20 µm high structures and on the substrate as well. This would be problematic with electron beam lithography, since keeping the sample in focus would be very difficult. This is why the Nanoscribe Photonic Professional was also used to do the lithography for the wiring. Because of the fact that laser lithography was used, the resolution was a lot worse, but with the large size of the structures the resolution was really not an issue. It was enough that the width of the wiring could be under a micrometre, which was possible even with the Photonic Professional. The advantage of using the Photonic Professional was its innate 3D capabilities, which made it easy to fabricate the wiring on different heights. Because the wiring was done with a lift-off process, a positive AR-P resist was used, and the DiLL method could not be used. I had to use an air-gap objective which was a LD Plan-Neofluar 63x/0.75 Corr M27 by Carl Zeiss. With this objective, the resolution is worse but now the objective does not have to touch the resist. Otherwise the method is similar to the DiLL method, where the focus is on the objective side of the substrate (Figure 11).

When doing the wiring lithography on top of already fabricated structures, the structures need to be found first with the optical microscope, integrated in the Photonic Professional. In this case, the Nanoscribe software has to be used to control the microscope instead of any external software, so that the next step is possible. After finding the structures, the coordinate system has to be aligned and the axis have to be scaled to the fabricated structures. This is done by selecting three spots on the structure, and then by giving

the coordinates of these points by hand. The Nanoscribe software then calculates the corrections it needs to do for the stage movements. This functionality is essential for this two-step process, because the size of the base structures changes because of the shrinking during development, and because the sample cannot be accurately aligned to the stage.

The parameters used for the lithography were otherwise the same as with the base structures, but now the tilt correction and the perfect shape were not used. The perfect shape could not be used, because with it the movement of the sample was too fast, and thus the dose was not high enough to expose the resist. Without the perfect shape, the speed is determined by the update rate and the point distance. The speed is the product of these two parameters. Different speeds were used in the tests, and the speeds were set by keeping the update rate always at 100 s^{-1} and changing the point distance so that the wanted speed was achieved. This was known to be a good way of controlling the speed from earlier experiments [40]. After doing the testing, I found out that a point distance of 150 nm worked well. This setting was used for all the later structures. Also different laser powers were used for the fabrication of the wiring. After finding the good speed settings, the laser power was used to define the width of the wiring. The used powers were between 50 % and 100% with a power scaling of 1. After the exposure, the development was done in a 1:1 solution of AR 300-47 and deionized water for one minute. When the minute had passed, the process was stopped by putting the samples in pure deionized water. As a last step, the samples were dried with nitrogen gas.

3.1.6 Evaporation and lift-off

Before the evaporation, a soft O_2 cleaning was done using an Oxford Instruments Plasmalab 80 Plus RIE (reactive ion etching) system shown in Figure 12C. This was done to make sure that there was no AR-P resist left in the lines created in this step. For the evaporation of the wiring a UHV (Ultra High Vacuum) evaporator by Instrumentti Mattila Oy was then used. The evaporator is shown in Figure 12D. It was first used to evaporate a small layer of titanium and then a thicker layer of gold. The reason for not evaporating only gold is the fact that gold itself does not adhere very well to a substrate, and thus the titanium layer is evaporated first so that the gold can adhere to the titanium. The evaporations were first done as a single angle evaporations from a 0° tilt angle (perpendicular to the substrate), and the film thicknesses used were 8 nm for the titanium and 50 nm for the gold. After it was found that the single angle evaporation did not create a good wiring the evaporation was changed to multiple angle evaporation. The problem with the single angle evaporation was that the films formed on the sloped surfaces of the samples were not continuous. The sequence for the multiple angle evaporations can be seen in Table 2. First the titanium was evaporated with all the different angles reading from top to bottom, and then similarly the gold was evaporated with all the different angles. This was the sequence used for all the later samples. The evaporation rate for both metals was always 1 Å/s.

After the evaporation, the lift-off was done using the AR 300-76 remover. The remover was heated on a hot plate, and the samples were kept in the hot remover throughout the lift-off process. This was done by using two beakers with the remover in them, and by switching the sample between the beakers so that at no point the sample itself was on the hot plate. If the sample would have been on the hot plate it could have been damaged by the heat. A common way of doing the lift-off is using a syringe to spray the solvent on the sample. This spraying technique was also used in this fabrication and it helps

Table 2: The angles and thicknesses used in the multiple angle evaporation.

Angle (°)	**Thickness of Ti (nm)**	**Thickness of Au (nm)**
± 75	1	3
± 60	2	5
± 45	3	10
± 30	3	10
± 15	4	15
0	6	30

a lot with removing the extra metal film. However simply doing the spraying was very time consuming. The sample had to be sprayed for over an hour, and there was always still some pieces of extra film left on the structures. To try to fix this problem also two other techniques were tried for the lift-off. The first technique was keeping the samples in boiling acetone. The idea behind this is that the bubbles forming on the sample will remove the extra metal film. The second technique was using a FinnSonic m03 sonicator to remove the extra film. The sonication was done as a very short burst, because it easily breaks the sample, as the sonication is actually a pretty rough technique.

3.1.7 Imaging and ion beam milling

The fact that both the sapphire substrates and the polymer structures are non-conductive made the imaging a bit harder. Luckily, the large size of the structures made it possible to use an optical microscope to learn a lot about the structures. The optical microscope used in this study was an Olympus BX51M. When a better resolution was required and when the studied sample was not going to be used for measurements, imaging was also done by first coating the sample with gold and then imaging with a SEM. The coating in these cases was done with a Jeol JFC-1100 ion sputter, because coating is very fast with this system, and because the quality and the thickness of the film do not really matter so much when imaging. The sputtering instrument is shown in Figure 12E. The parameters used were: current $I = 10$ mA and voltage $V = 1$ kV, and the coating was done for 30 seconds. The SEM used for the imaging was a Zeiss Leo 1430, because its stage can be tilted and rotated, which allowed easy imaging from different angles. The resolution of this SEM is not at the level of more state-of-the-art systems, but it was good enough for the samples made in this study. The SEM is shown in Figure 12G.

For ion beam milling and imaging at the same time, a Zeiss Orion Nanofab HIM (helium ion microscope) was used. The system is shown in Figure 12F. The only images taken with the system were the images of the milled samples, because this system was very new and less available for use. The advantage of using this system for imaging the samples of this study is its capability to image samples that are non-conductive, because of the electron flood gun used in the system. This flood gun is used to neutralize the sample, and thus avoid the charging effect, which normally makes imaging nonconductive samples impossible. This system also has a better resolution than any of the SEMs in the Nanoscience Center. When doing milling, neon gas is used instead of helium, which is used for imaging. This is because neon ions are heavier than helium ions and thus mill a lot faster. When doing the milling, the beam current was set to about 100 pA and the used aperture was the Neon 70 µm aperture.

Figure 12: The devices used in the fabrication of the structures. A, Nanoscribe Photonic Professional. B, Beneq TFS200 ALD. C, Oxford Plasmalab 80 Plus RIE. D, UHV evaporator. E, Jeol JFC-1100 ion sputter. F, Zeiss Orion Nanofab HIM. G, Zeiss Leo 1430 SEM.

3.2 Measurement setups

3.2.1 Probe station

In this study, the resistance of the samples were measured at different temperatures from room temperature down to at least a temperature, where the resistivity of gold turns constant as a function of temperature. This temperature is typically around 20 K [42]. Two different measurement setups were used for measuring the resistance of the samples as a function of temperature: the first of these was a Janis CCR-10 cryogen free probe station. This system is shown in Figures 15A and B. This system can reach a temperature of 10 K with pulse tube cooling, and can reach a vacuum of 10^{-6} mbar. In this system, the connection to a sample is created with micromanipulated mechanical probes. These probes can be directly connected to the connection pads on a sample, or the sample can be first connected to a circuit board which then has bigger pads for the probes. In early test measurements I found out that if the probes were directly connected to the pads on the sample, the connection was very unstable. This was because the probes could not be connected with a lot of force or they would break the delicate bonding pads. Then when the temperature went down, the contact disappeared due to the thermal contraction of the probes. This problem was fixed by first bonding the sample with aluminium bonding wire to a copper circuit board with large bonding pads. Then, the probes could be connected to the circuit board with enough force to make sure that the contact did not break during the measurement.

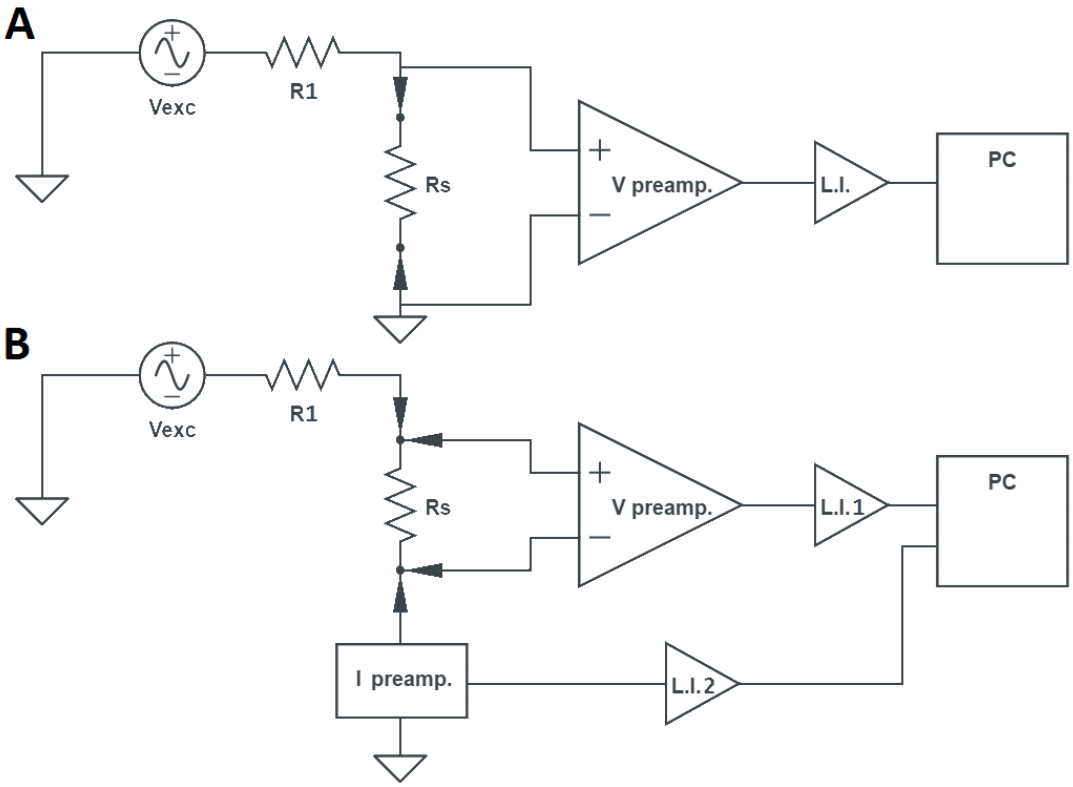

Figure 13: The circuits used for the resistance measurements. A, the two probe circuit used in the probe station measurements. B, the four probe circuit used in the probe station and the dip stick measurements. L.I. is an abbreviation of lock-in amplifier. The positions of the probes are marked with the filled-in arrowheads.

The circuits used for the probe station measurements are shown in Figure 13. The voltage preamplifier was a DL instruments 1201 and the current preamplifier was a DL instruments 1211. The settings for the voltage preamplifier were gain = 100, high pass = 0.3 Hz and low pass = 100 Hz. The same settings were used in all the measurements. For the current preamplifier the setting were sensitivity = 10^{-4} A/V, suppression = 10^{-3} A and rise time = 1 ms. Similarly to the voltage preamplifier, the settings were the same for all the measurements. For the probe station measurements, the two lock-in amplifiers were both Stanford Research systems model SR830 DSP lock-in amplifiers. One of the lock-in amplifiers measures the voltage, and the other measures the current. The settings for the lock-in amplifiers were different for different measurements. The V_{exc} signal was taken from the internal source of lock-in amplifier measuring the voltage, and given as an external reference to the other lock-in amplifier. The used equipment is shown in Figure 14A. The resistor R1 had a value (33.2 ± 0.3) kΩ, measured with a Fluke 175 TrueRMS multimeter. The temperature in the probe station is measured with a Lakeshore 336 Temperature controller. The signals from the lock in amplifiers and the thermometer were routed to a computer through a National Instruments connector block and a National Instruments PXI ADC card system. The data was collected on the computer using an in-house made LabVIEW program.

3.2.2 Dip stick

The other setup for the resistance measurements was a dip stick system. In this setup, a stick with a sample stage and connectors shown in Figures 15B and C is lowered slowly to liquid helium. The liquid helium is in a large dewar that is shown in Figure 15D. The stick can be connected to the top of the dewar, and then a seal can be used to tighten or loosen the stick so that it can be moved up and down and also kept at a constant height. The cooling measurements were done simply by lowering the sample in small increments into the dewar, and letting the sample cool slowly between the increments. The heating measurements were done similarly but the sample was just lifted instead of lowered. Because liquid helium is used for the cooling, with this setup a lower temperature of about 4 K could be reached. In this setup, the sample had to be directly bonded to the stage shown in Figure 15E, which of course made this a very stable measurement.

Figure 14: The devices used in the measurements. A, devices used at the probe station. Lock-in amplifires on the bottom left and preamplifiers on the right. B, different lock-in amplifiers used with the dip stick.

The circuit used for the dip stick measurements is the circuit in Figure 13B, which is the four probe circuit also used in the probe station measurements. The equipment was otherwise the same but this time the lock-in amplifier measuring the current was a Signal Recovery model 5210 lock-in amplifier. The equipment is shown in Figure 14B. The settings for the lock-in amplifiers were different for different measurements, but the settings for the preamplifiers were the same as in the probe station measurements. In this dip stick setup, the temperature was measured using a resistive temperature sensor on the sample stage, which was measured with a Picowatt AVS-47 Resistance Bridge. This temperature sensor was in-house calibrated. The signals were recorded on a computer with a similar setup as with the probe station, but this time the connector block was a National Instruments BNC-2090. Similarly to the probe station, the data was collected with an in-house made LabVIEW program.

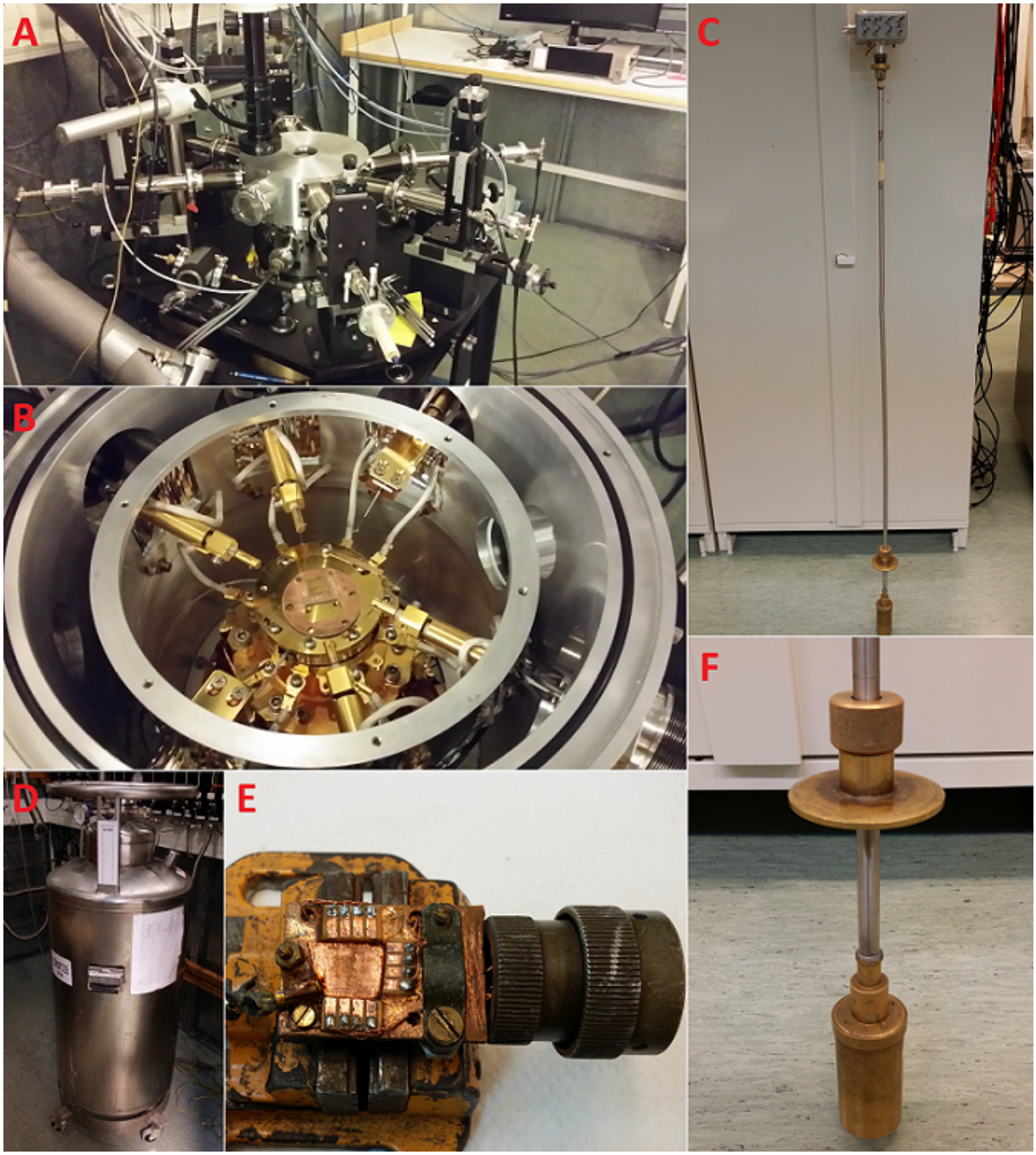

Figure 15: Measurement setups used in the resistance measurements. A, the probe station. B, close up of the sample stage in the probe station. C, the dip stick. D, the dewar for the liquid helium. E, the sample stage used in the dip stick. F, close up on the sample holder and the attachment part of the dip stick.

4 EARLIER RESULTS

I have also studied parts of the fabrication process earlier. These earlier studies focused on the 3D fabrication of the base structures for the parallel plate geometry. In the earliest studies it was found that when using the DLW method in the 3D-lithography, there is an issue with the laser power due to the laser going through the sample [19]. This is why in later experiments the DiLL method was used, the base structure design was formalized and the ALD coating tested [20]. The ALD tests were successful on the structures themselves and the fabrication was otherwise successful, but the smallest gap size reached was (2.2 ± 0.2) µm [20] not quite in the nanoscale. The reason why a smaller gap could not be achieved is the shrinkage of the resist which happens in the development phase. This is a well-known issue, and Nanoscribe GmbH even reports how bad the shrinkage is for their different resists [41]. Since the base structures had been already well developed, this study focused more on the fabrication of the wiring, thus proving that this kind of system could be used for the near-field heat transfer measurements. Some efforts were also taken to create a smaller gap, but this was not the main focus. The near-field experimental structure consists of two cuboid structures, which are made with the 3D-lithography, as shown in Figure 16. Here we designed a process which can be used to fabricate a heater and a thermometer on the 3D structures and the associated wiring for these devices.

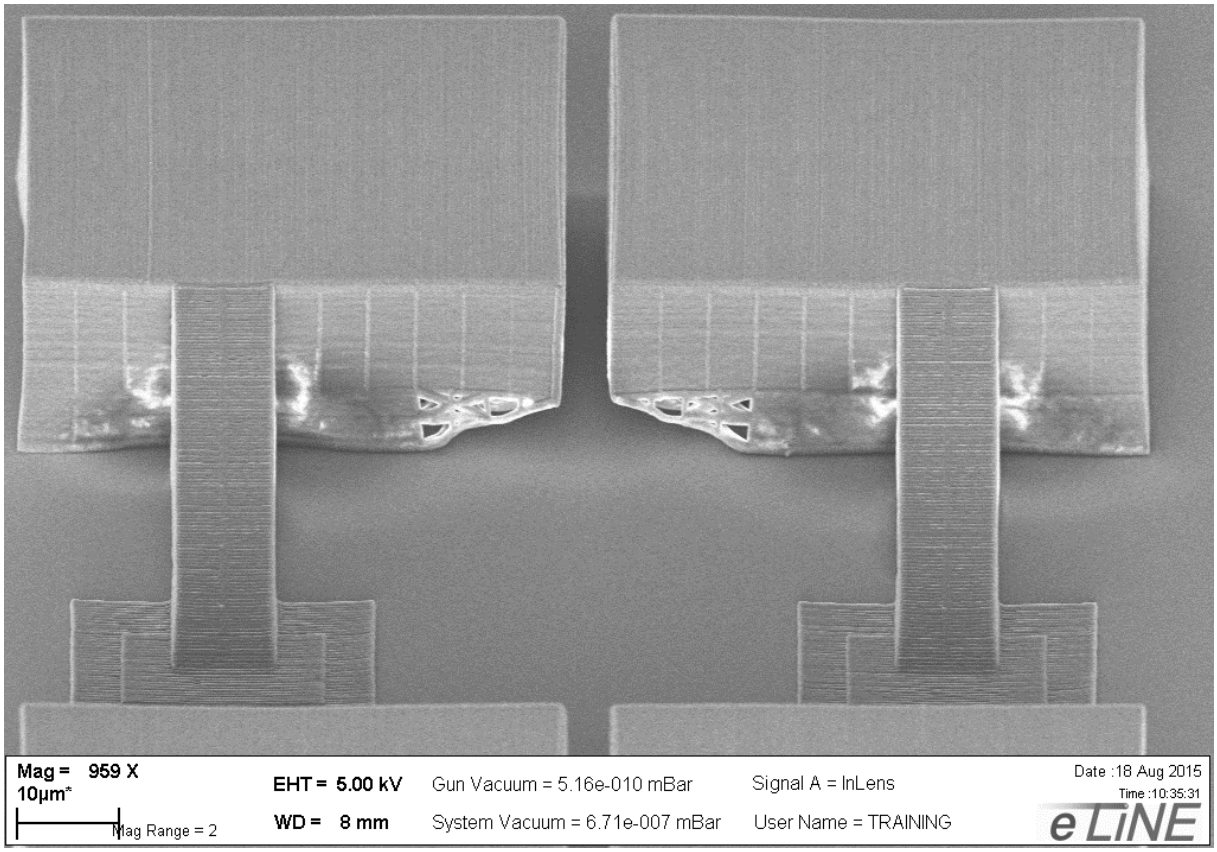

Figure 16: The base structure imaged with a scanning electron microscope.[20]

The structure shown in Figure 16 is the culmination of the earlier studies. The size of a single cuboid structure is 55 µm x 40 µm x 20 µm, where the last dimension is height. As can be seen from the Figure 16, there are ramps meant for the wiring and the parallel walls forming the gap have been suspended from the substrate. The suspension is done because the substrate is planned to be etched away from between the structures for the actual heat transfer measurements. This has to be done to minimize the direct heat flow through the substrate. The plates at the bottom of the slopes are there to work as anchors for the slopes, because without them, the slopes were suspended above the substrate due to the shrinkage of the resist. From Figure 16 it is also apparent that the parallel walls are not totally straight. It is extremely hard to make the walls straight, because of the shrinkage which bends the walls slightly. To get the walls to be even as straight as in Figure 16 dozens of experiments with different compensations in the design were required.

5 RESULTS

5.1 The wiring lithography process

The process that was used for the fabrication of the wires was laser lithography and lift-off. Because of the large height of the structures, or more accurately because of the large variations in the height, the lithography had to be done using the Nanoscribe Photonic Professional instrument instead of e-beam or UV lithography. The Photonic Professional is designed for 3D-lithography so doing normal 2D laser lithography with it on different heights is quite easy. The use of Nanoscribe allowed the fabrication of all the wiring on the structures and on the substrate in one go. The decision to use the Photonic Professional for the lithography forced me to use AR-P resist, which was the only positive resist that we knew would work with the system, because it had been tested a year earlier [40]. With the AR-P resist, an air-gap objective is used because the AR-P resist is a solid resist, and thus the objective cannot be in contact with the resist as it is with the liquid dip-in resist. The air-gap objective has a lower resolution than the other objectives, but the resolution is high enough for this process because of the large size of the structures.

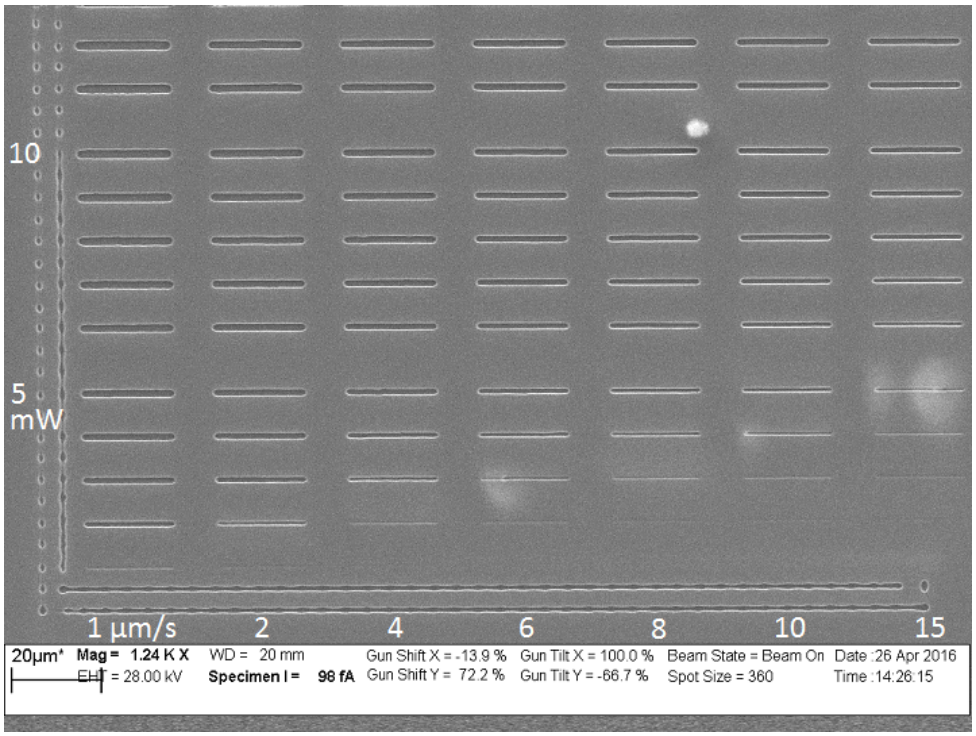

Figure 17: A test pattern imaged with a scanning electron microscope. The length of the lines is 20 µm. Laser power varies on the y-axis and speed on the x-axis.

To do the lithography on top of the structures, the lithography has to be done from the top side of the structures, so that the laser does not go through the substrate. This is similar to the DiLL method. The earlier experiments [40] had all been done through the substrate with the DLW method, so first I had to test if the lithography even works the

other way around. So at first I just spinned the resist on a sapphire substrate and made some test patterns. These patterns consisted of lines which were drawn with different speeds and laser power values. First the spinning was done at 1000 RPM for 60 seconds which should produce a 1 µm layer but this did not produce an even layer of resist. There were large thicker patches of resist on the substrate. This was probably due to the small size and square shape of the substrates which caused the resist to accumulate on the edges of the substrate. Because of this problem, the speed was changed to 1500 RPM to produce an 800 nm layer of resist, and the time was changed to 90 seconds to make sure that the resist had time to flow on the substrate as much as possible. With these parameters, there were only very small thicker patches on the corners of the substrate, which is not a problem since the basr structures are located in the middle of the substrate. To my surprise, the Photonic Professional was able to find the resist interface automatically and the lithography worked well. An exposed and developed test pattern is shown in Figure 17. From the figure it can be seen that the lithography worked well because the lines are developed all the way through the resist layer. So from this result I knew that the spinning parameters were appropriate, and I also found out what kind of speeds and laser powers could be used for the lithography. In addition, this result showed that the required line width could be reached with this process, because some of the lines had a width of less than one micrometre.

After it was known that the lithography worked, the lift-off process could also be tested. To test the lift-off, one of the test patterns was coated with 8 nm of titanium and 50 nm of gold using the UHV evaporator. The lift-off was done normally by spraying the remover solution using a syringe. The result is shown in Figure 18. From the figure, one can see that the lift-off works pretty well and even most of the smaller lines were intact. Now that it was known that both the lithography and lift-off worked on the substrate, it was possible to continue with the project. These tests really had to be made because this specific process had never been tested, and also as the AR-P resist is not really designed for the Photonic Professional. It was also known that the lift-off process can be quite difficult with this resist.

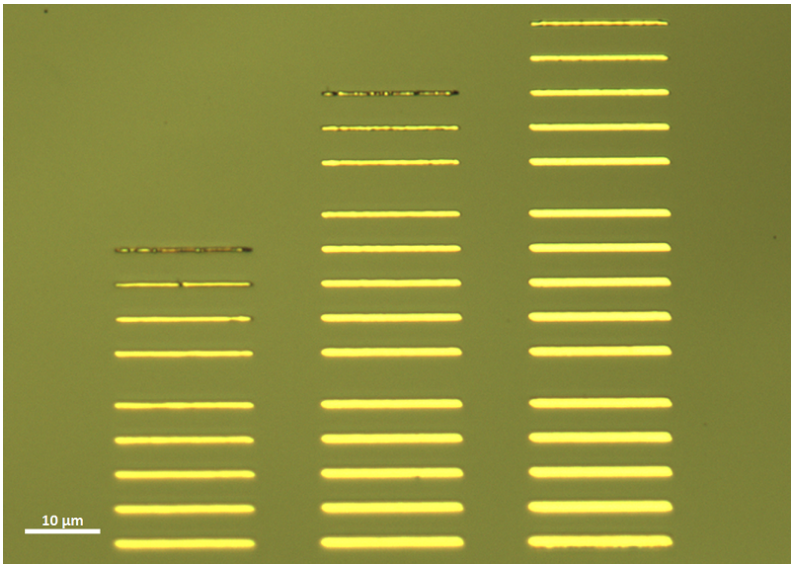

Figure 18: Gold lines on the substrate after the lift-off process. The length of the lines is 20 µm. Imaged with an optical microscope using a 50x objective.

5.2 Coating a fabricated structure with resist

As the lithography for wiring was tested and it worked on flat surfaces, I could test the two step process, in which the lithography is done on a three dimensional structure. I started these tests by first designing a simple base structure, which was a 10 µm high cuboid with slopes on two of its four edges. This structure was fabricated using the normal DiLL method. For the actual measurement samples the next step would be the ALD but since I was just testing the lithography process first, the ALD was skipped, making the process much faster. So the next step was spinning the resist, and this was done using the same parameters as in the first test. At first, I only used a single 800 nm layer of resist. Then I used the Photonic Professional to draw a simple test pattern that had lines both on the structures and on the substrate. After the development, I coated the test sample with gold using the plasma coater so I could image it with a scanning electron microscope. Figure 19 shows one of the test structures. It can be seen that there are lines on the slopes and on the substrate, but there are no lines on top of the main structure. One can also see that the depth of the lines on the slopes gets smaller when the slope gets higher. Finally at the top of the main structure the lines vanish, and one can see a flat base structure everywhere. So the image shows that there is no resist on top of the main structure. This was an unexpected problem and I had to start thinking of ways to fix it.

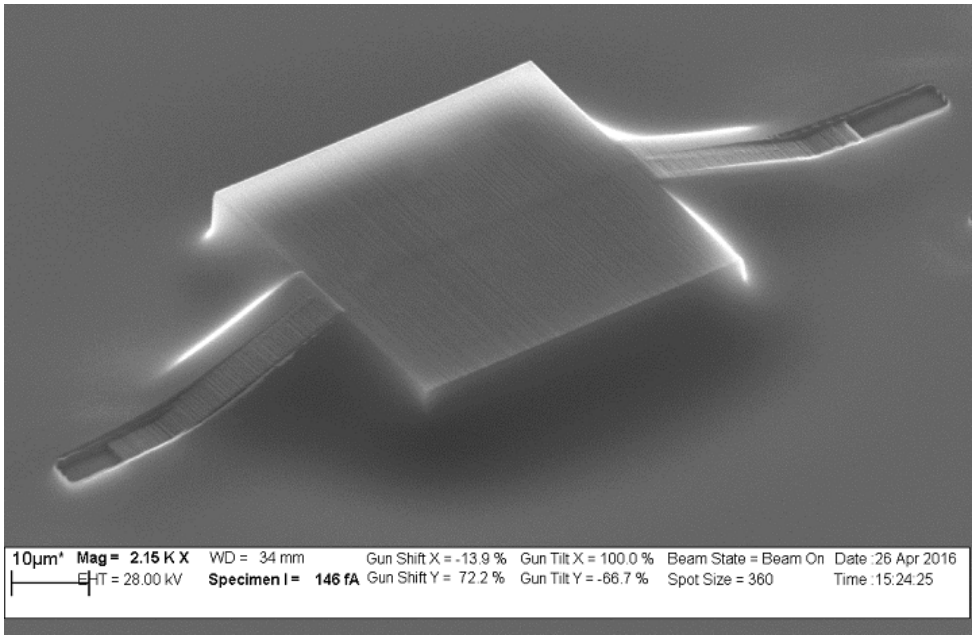

Figure 19: The first lithography test on top of a 3D base structure. The width and length of the structure is 50 µm and the height is 10 µm.

First, I tried the simplest possible fix, adding more resist layers on the structures. Also at the same time I tested if just letting the resist sit on the sample before the spinning helps. The thinking behind this is that the solvent in the resist has some time to evaporate and the resist will stick better on the structure before the spinning. So I first pipetted the resist on a sample and let it set for 10 minutes before the first spin. Then I spinned three layers of resist on the sample using the same parameters as for the single layer spins. Of course the sample was baked after every spin. When spinning multiple layers of resist the sample is exposed to more heating. This heating has an effect on the base structures which can be seen in later images, but there are no large changes in the structures. In

Figure 20 there is a sample with three layers of resist, which has similar patterns as the sample in Figure 19 fabricated on it. As can be seen by comparing the Figures 19 and 20, the result is quite similar even with multiple layers of resist. There is now a very thin layer of resist on top of the structure in Figure 20 as can be seen from the faint lines created with the lithography. However, the layer is way too thin to actually work for lift-off, and there would be even less resist on one of the actual base structures, because they are twice as high as these test structures. This small layer of resist on the structure is perhaps left on the surface due to the waiting time before the spinning, as then the resist has time to adhere to the surface better. At this point, it became clear that just spinning the resist on a 3D base structure would not work for this process.

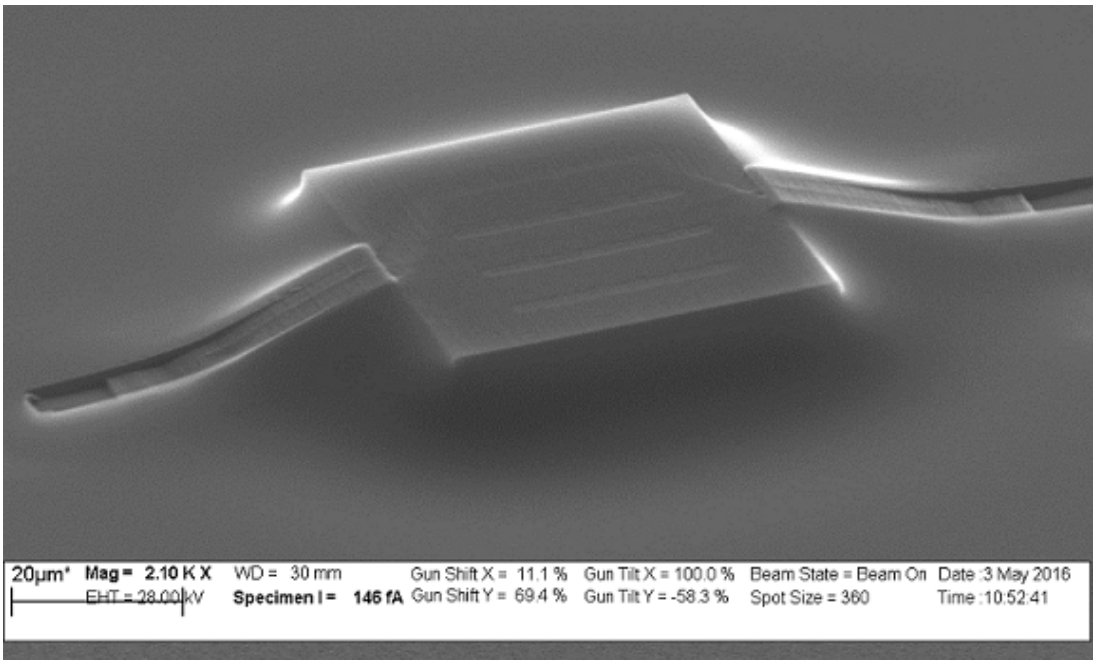

Figure 20: Lithography test on structures with three layers of resist. The structure is similar to the one in the first lithography test.

The next possible fix was to try a different coating method. Probably the best method to use would be spray coating, as it has been shown to work on samples with very high topographical steps, for example by K.A. Cooper et al. [43]. Interestingly, in the same study they had arrived to a very similar result with spin coating as I did. Spray coating was however not available for me. Since I could not try it, the only other option was dip coating. So I made a similar test sample and coated it with the same AR-P resist using a dip coater. The withdrawal speed used in the coating was 10 mm/min. This speed was chosen according to results gotten by P. Yimsiria and M.R. Mackley [39] with solutions that had a similar viscosity. After the coating, the lithography was done similarly as in the earlier experiments. The finished sample can be seen in Figure 21. As can be seen in the figure, the result is very similar to the spin coating. There are no lines on the top of the structure and you can definitely see the top of the structure. No lines were drawn on the ramps of this specific structure. The result could perhaps have been better with a faster withdrawal speed, but the used speed was already pretty much the top speed of the coater. There was a possibility to set a higher speed but then the coater could not keep the speed constant anymore. So from this experiment, it became clear that dip coating would not fix the problem at least with this coating system.

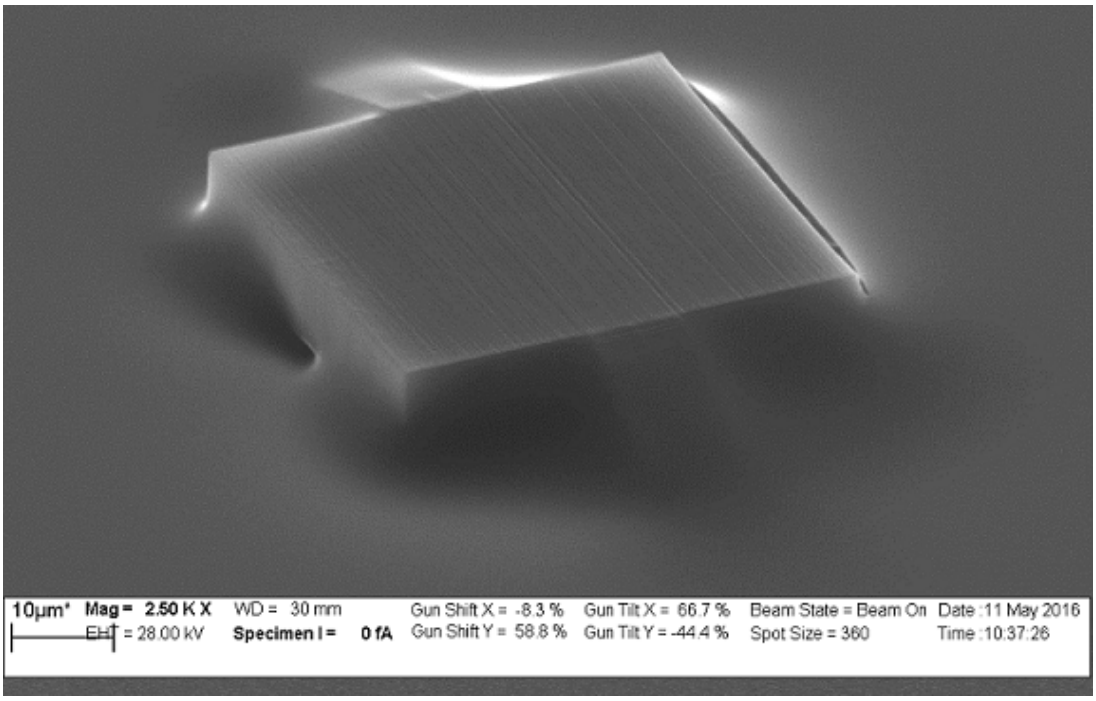

Figure 21: Lithography test on structures that were coated using dip coating.

Since the available coating methods did not produce the wanted result, some workaround had to be found. Basically the only choice at this point was to change the base structure in some way. The workaround I came up with was very simple. I decided to make small walls which enclose the top of the base structure creating essentially a bowl for the resist to stay in, see Figure 10. I left small holes in the walls at the points where the ramps are, so that the wiring can go through there. Then I did spin coating and the lithography in a similar way as before. The result is shown in Figure 22. In this first test, the height of the walls was about 2.6 µm and the width about 0.6 µm. Now as can be seen in Figure 22 there are lines also on the top of the structure which means that the workaround was successful. The lines on top are also pretty deep so there is quite a thick layer of resist on the structure. The only part where the thickness of the resist layer is very thin is at the top of the ramps. The resist is so thin here that it is an issue for the lift-off as will be shown later, but this is only a very small issue since we don't really care how wide the wires are on the ramps. The other small issue with this walled structure is the top of the walls. There is no resist left on the top of the walls, which can be seen in Figure 22. This problem will be elaborated on in the lift-off section. In all other places, however, the resist is thick enough for lift-off which meant that the project could advance to the next phase.

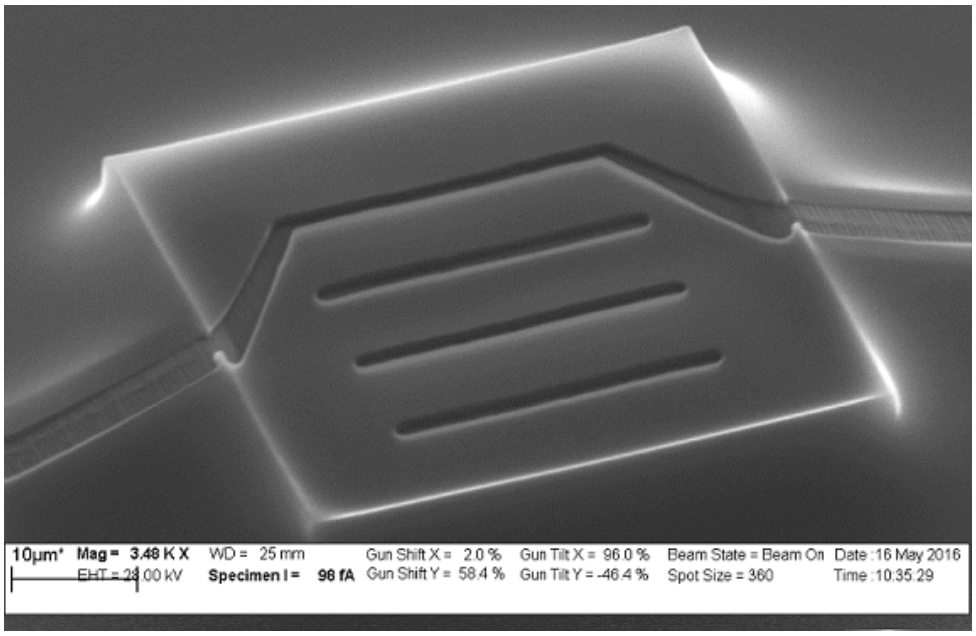

Figure 22: Lithography test on a structure with walls surrounding the top. The structure is the same as before with just the walls added. The height of the walls is about 2.6 µm.

5.3 Metal deposition and lift-off on a fabricated structure

The next phase was the lift-off process, to create the actual wires on the structures. For the lift-off tests, the lithography was done similarly as for the earlier tests, but the patterns that were drawn were simpler, and four layers of resist were used instead of three. The drawn patterns consisted of a single wire that has a narrower section on the structures, see Figure 23A. This narrow wire section on top of the structures will then work as the resistor in the finalised sample. The used base structures were similar to Figure 16 but with the walls enclosing the top and slopes on both sides. This meant that the structures were twice as high (20 µm) as the ones used for the lithography tests. Before the lift-off, the developed samples were cleaned by doing an oxygen cleaning with a RIE. After the cleaning, first titanium and then gold was evaporated on the sample using the UHV evaporator. For the first test, 8 nm of titanium and 50 nm of gold was evaporated at a 0° angle. Then, the actual lift-off was done by spraying the remover solution on the sample using a syringe while the sample was kept in the heated remover solution. Two of the structures on the first successful sample are shown in Figure 23B. To get the result, the lift-off had to be done three times. That is because the lift-off was difficult to do and the structures broke very easily. The gold layer is hard to remove because there is no undercut along the walls of the developed lines, and thus the lift-off took over an hour to do. Also, as can be seen in Figure 23B, there are easily small bits of gold film left attached to the walls and the ramps. The top of the walls are also totally covered in gold after the lift-off, and the walls have clearly been bent in the process. This means that there will be another wire along the walls which is parallel to the actual resistor wire. Even though there was still a lot to improve upon, this result gave hope that the lift-off can be done.

Because the lift-off was so hard to do, I tested different ways to do it. The first thing that I tested was just putting the sample into the heated remover solution immediately after taking the sample out of the UHV. This seemed to help a little, but still the remover had to be sprayed for a very long time. Another thing I tested was making the structures

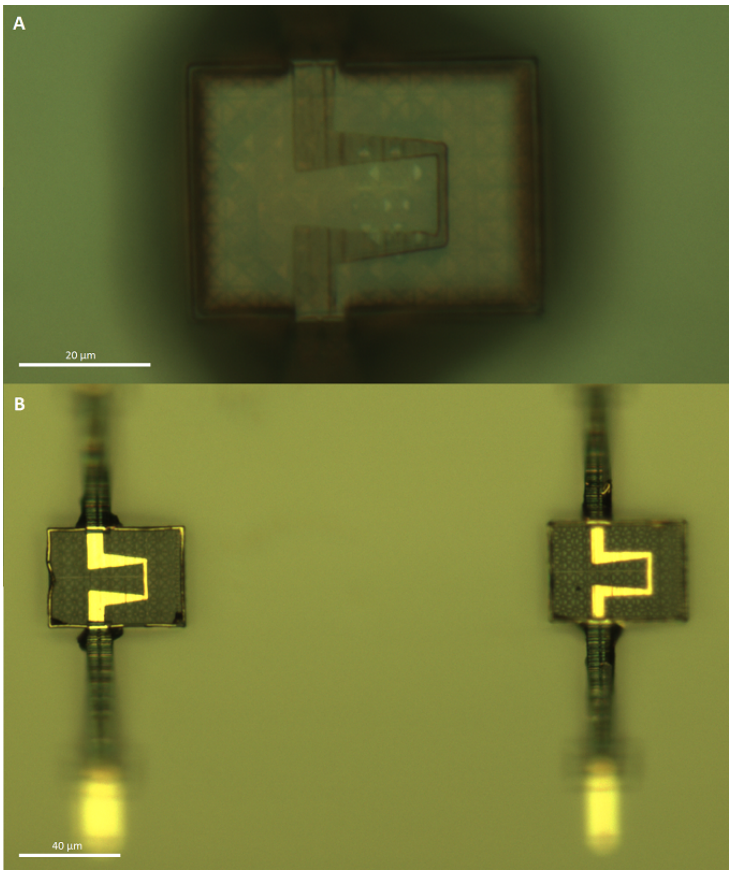

Figure 23: Lift-off test on an actual base structures with walls enclosing the top of them. A, one structure after development. B, structures after lift-off.

larger so the wires would be farther away from the walls. So I did tests with structures which were 20 µm wider. This made a large difference and cut the lift-off time to about half of the original time. With the smaller structures the lift-off sometimes did not work at all, but with the larger structures the lift-off worked to some degree every time when the structures did not break. Doing sonication instead of the spraying was also tested, but the sonication was way too rough and also removed the whole base structures from the substrate, even if the sample was just dipped in the sonicator very quickly. Another method that was tested was keeping the sample in boiling acetone but this had no effect. So, the only option was to continue doing the lift-off by spraying the remover.

The next step was to find out if there was an electrical connection across the sample. For the test a sample with contact pads had to be made first. So I fabricated a similar sample to Figure 23B but with added contact pads, and also two different sizes of base structures. For these tests, two base structures were also put close together to create the gap, with a design gap width of around 2 µm. All the fabrication steps were the same as before, and the lift-off was done so that the sample was put into the heated remover solution immediately after the evaporation. A final sample is shown in Figure 24. As the image shows, the pads came out well and there was no problem with the lift-off on the substrate, but again there was still some extra gold film on top of the structures. Another thing that can be seen in the figure is that the two structures are connected to each other. This happened because the small walls bent during the process, and the two walls along the gap collapsed on each other. The walls were simply not strong enough.

This bending happens during the evaporation and lift-off, since the structure gets hotter during evaporation, and mechanical stress is introduced in the lift-off. I can be sure that the bending happens during the evaporation or lift-off because after the development, the walls are still straight. There was also an issue with the lift-off at the bottom of the ramps in some of the structures as can be seen in Figure 24C. Basically a part of the actual wire is lifted-off, which happened because that spot had not been exposed enough in the lithography, and thus there was some resist left there after the development. On top off all the other problems, there was no electrical connection across the sample. The connection was tested simply by using a multimeter with probes which can be accurately manipulated to contact the pads. The reason why there was no connection was probably because the 0° angle evaporation did not create a good film on the ramps.

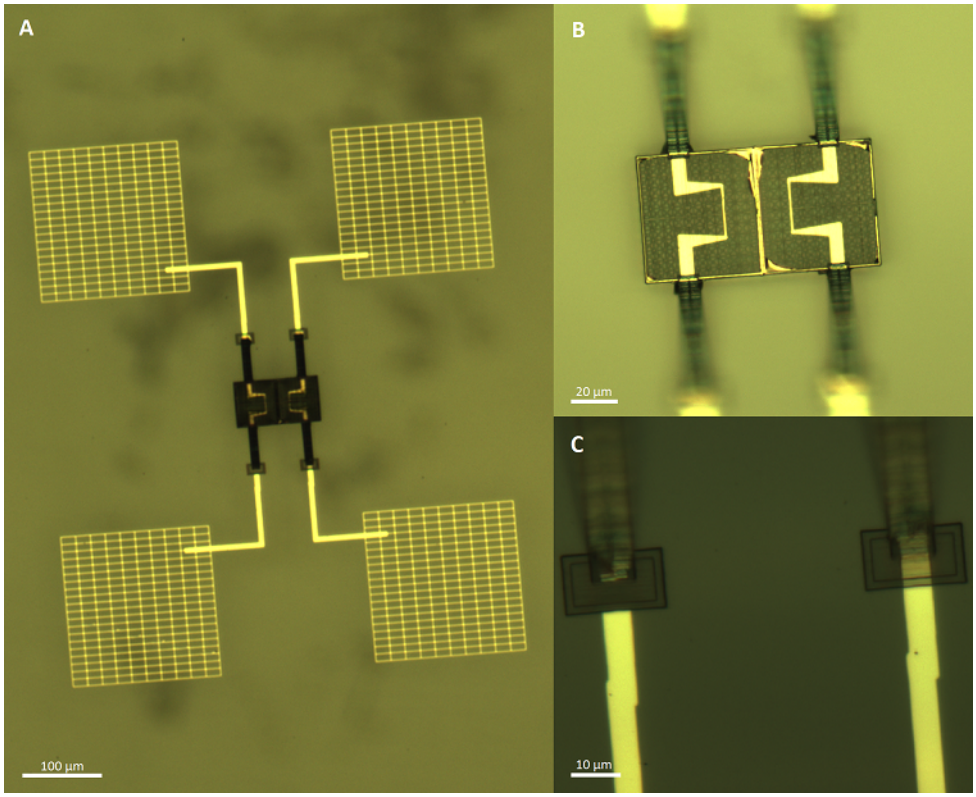

Figure 24: Lift-off test on base structures with gold wiring and walls enclosing the top of them. The wiring on the ramps exists, but is not visible due to the angle of view.

With all the information from the previous tests a better sample was designed. This time the walls on the structure were made so that they were tilted inwards as shown in Figure 25A, making it impossible for them to collapse on each other, and at the same time possibly providing an undercut for the lift-off. Also the evaporation of the metals was changed so that it was done from multiple angles to ensure a connection across the ramps, according to the sequence discussed in section 3.1.6. The resulting sample is shown in Figure 26. It is clearly apparent from the figure that the tilted walls made the lift-off result actually worse. This is partly because of the multiple angle evaporation, which resulted in no undercut even with the tilted walls, however, the biggest problem is the increased surface area provided by the side of the tilted wall. A large amount of extra gold got stuck on the side of the tilted walls. So the tilted walls were not a good solution. However, now there was an electrical connection across the sample, which means that the multiple angle evaporation worked. Because of the large amount of extra gold, the

current could flow even over the gap, but still, this result showed that there was now a better gold film on the ramps.

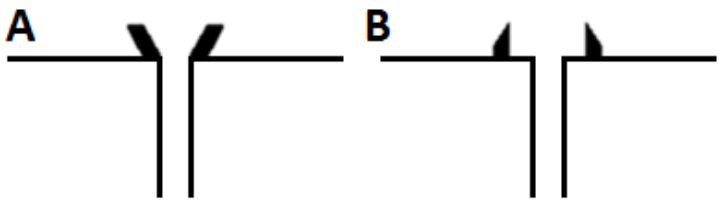

Figure 25: Schematic cross-section of structures with two different wall designs. A, walls tilted inwards. B, shifted walls with a slope on the inside.

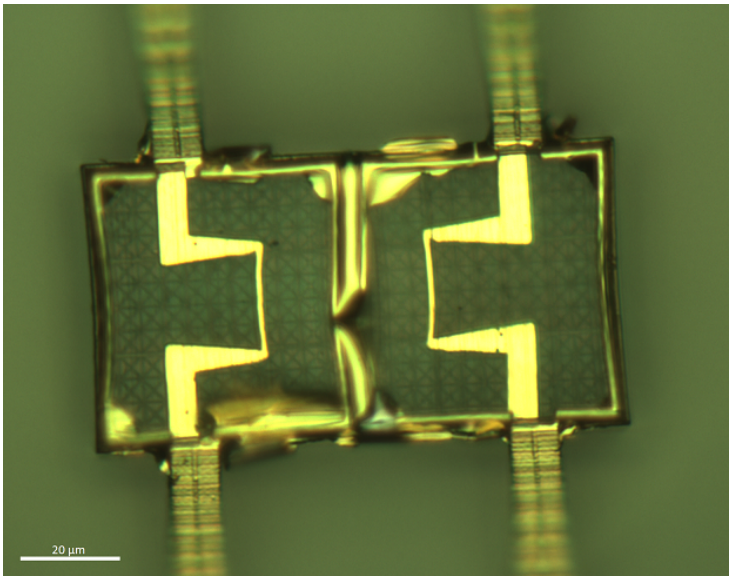

Figure 26: A sample with the top walls tilted inwards. Gap formation was not successful, because of the extra gold in between the structures.

Since the tilted walls did not work, I went back to straight walls, but for the next test I made the walls farther apart at the gap by shifting them inwards from the gap edge. This should guarantee that the walls cannot collapse on each other. Having a wider gap between the small walls should also improve the lift-off between the structures, and thus break the connection between the structures. Another thing that I tested was to make the top of the wall thinner, by making a slight slope on the inside edge of the walls as shown in Figure 25B. With this design the width of the base of the wall was about 0.8 µm, whereas the top was about 0.2 µm wide. At this point, the ALD step was also included in the process. So now all the base structures were coated with 50 nm of Al_2O_3 after their development using ALD. This step makes the structures mechanically stronger which should also help the lift-off. So the ALD step could help with removing the extra gold left on the structures, since now rougher lift-off techniques could maybe be used.

The results of these two tests are shown in Figure 27. As can be seen from Figure 27A, the larger distance between the walls removed the extra gold film between the structures, but still there was extra gold remaining on the walls in other parts of the structure. When the walls were sloped so that there was less area for the gold to adhere to (Figure 27B), there was more or less no extra gold left on the walls. The only part where there is some

extra film is at the beginning of the slopes, but this is not an issue since there the wires are a lot wider than on the structure anyway. The ALD step also improved the lift-off result. This is because with the stronger structures, even very short sonications could now be made during the lift-off, helping a lot with removing the excess gold film.

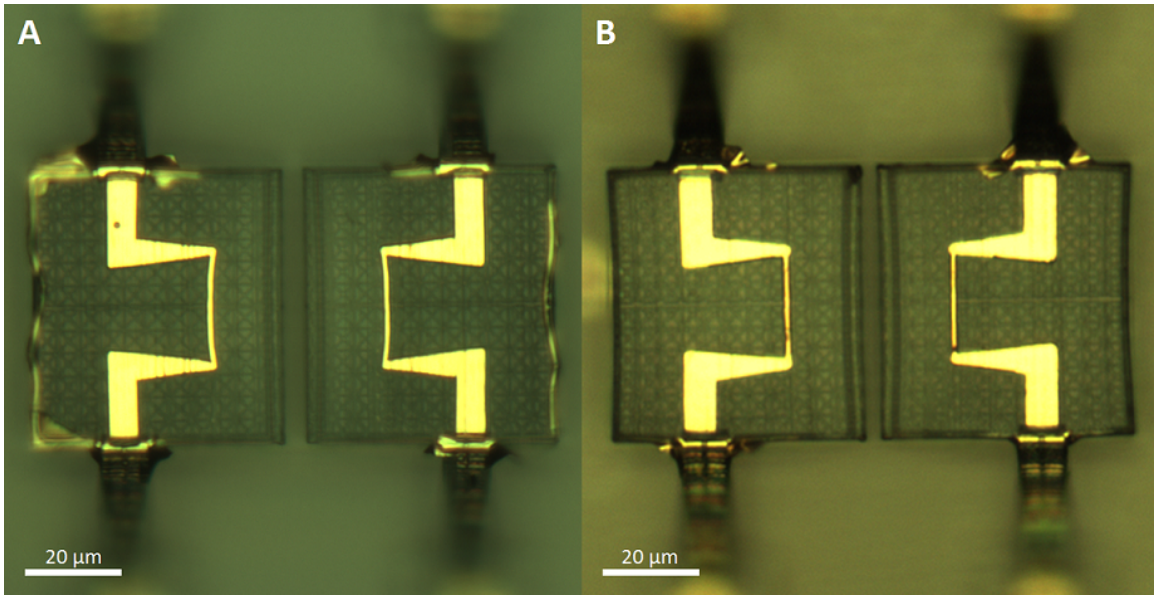

Figure 27: A, a structure with the small walls shifted 2 µm inwards from the gap edge, and a design gap width of 2 µm. B, similar structure with the walls sloped on the inside. Both samples were coated with 50 nm of Al_2O_3 before metal deposition.

5.4 Making the gap smaller with ion beam milling

The smallest gap in the structures that were fabricated with the above methods was about 3 µm wide. However several theoretical results have shown that at room temperature, the near-field heat transfer becomes dominant only when the gap size is under 1 µm [4][5]. As I mentioned in section 4, it has been impossible to make the gap smaller than 2 µm using just the Photonic Professional because of the shrinkage happening in the resist. Thus, some different ways to make the gap smaller need to be investigated. One possibility is to change the whole design of the structure, but this would be a very time consuming way to try and find a design that would work. Another way we came up with was to make a similar structure that I have been using, but make it so that the two structures are first connected, and then mill them apart using a HIM. Making the structures so that they are connected to each other means that the shrinkage cannot pull the structures apart in the development phase. The connection was achieved by adding connecting beams between the structures that could easily be cut later using ion milling. At the same time, I made the gap smaller than before in the design to see that the beams also keep the structures from being totally connected to each other. I made two samples with different sized beams to see how strong the beams would have to be. The cross sections of the beams were 0.5 µm x 0.5 µm and 1 µm x 1 µm. For this test, the structures were not coated with ALD.

In the sample with the thinner beams, the beams broke during the development due to the shrinkage of the structures. However, the sample with the wider beams was successful, and some of the structures are shown in Figure 28. As can be seen, the structures were only connected by the beams, which means that the beams allowed the gap to be smaller.

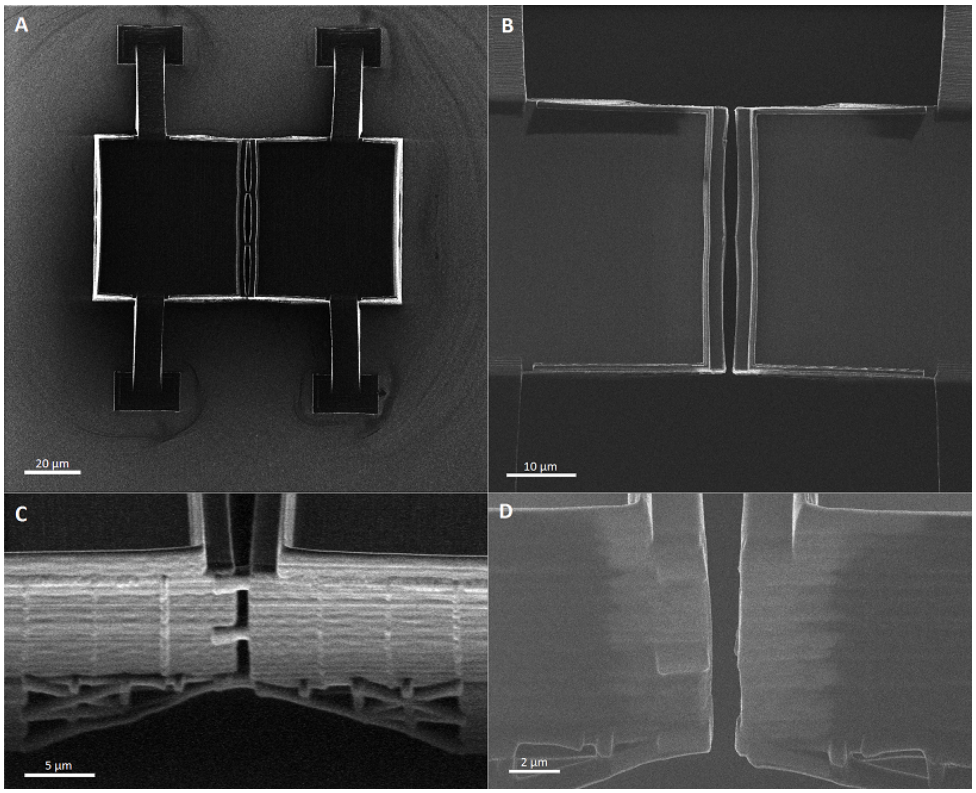

Figure 28: Structures imaged with a HIM. A, a 60 µm wide structure with a gap size of (2.35 ± 0.05) µm before milling. B, a 40 µm wide structure after milling. The width of the gap is (1.97 ± 0.05) µm. C, a close up of the connecting beams, side view. D, a close up on milled beams, side view. The quality difference between the images comes from the fact that the images A and C were taken with neon, but B and D with helium.

However, as can be seen in Figures 28A and 28B, the wall bends between the beams, and even after cutting the beams the wall does not straighten up. This is a big problem since the walls should ideally be as straight as possible. This problem could probably be fixed by using entire planes to connect the structures but this would make the milling take a much longer time. Already now, the milling took over an hour for a single structure. However this would be a good option to study in future experiments, and perhaps some better designs for the structures could be designed to make the milling faster. For now, this result shows that this cutting is possible, and it is apparent by comparing Figures 28C and 28D that the milling works very well. The beams are totally removed and the main structures themselves are not affected at all.

In addition to taking the images, the gaps were measured before and after the cutting at the spot where the gap was widest. The milling was done to two structures, one which was 40 µm wide and the other was 60 µm wide. The height of both structures was 20µm. The results were (2.35 ± 0.05) µm before and (2.66 ± 0.05) µm after for the 60 µm wide structure, and (1.32 ± 0.05) µm before and (1.97 ± 0.05) µm after for the 40 µm wide structure. The errors come from taking the measurements just from the HIM images. In both cases the gap gets larger by about half a micrometre. This tells us that there is still some tension in the structure after development, which is released when the beams are cut. The tension is problematic since it means that probably a gap smaller than 1 µm will not be possible with this design. This is because the gap can only be made to be

about 1 µm before the cutting. However, the gap of (1.97 ± 0.05) µm is the smallest gap achieved for a full sized structure, meaning that so far this milling technique seems to be the best way to make the gap possibly even smaller in the future.

5.5 Resistance measurements with the probe station

Now that samples with working wiring had been fabricated I was able to start measurements. It was important to first get good results from the lift-off to make sure that the current will only go through the intended wire, so that correct values would be measured. Since the samples were to be used as a heater and a thermometer, we wanted to measure the resistance as a function of temperature. The measurements were started with the very simple two probe setup (Figure 13A) with the probe station discussed in section 3.2.1. In this setup just the voltage over the sample was measured, while the current was kept constant. The measurement was done so that the voltage was measured while the sample was cooling and heating. The settings used in the lock-in amplifier were V_{exc} = 0.332 V, sensitivity = 100 mV and time constant = 300 ms. The resistance of the sample R_S was calculated from the known current $I = V_{exc}/R_1$ and the measured sample voltage, by using Ohm's law $R_S = V_s/I$. The results of the first measurement are shown in Figure 29. It is immediately apparent that there is something strange about the result. As Figure 29 shows, at high temperatures the resistance is linear in temperature as expected with a metal wire. However, when the temperature is below 125 K something weird happens. When the sample is cooling (measurement 1) the resistance suddenly shoots up and then does not continue linearly anymore. Interestingly, the curve is also different when the sample is heating (measurement 2) showing a hysteresis between the curves. This is not what should be happening when measuring a metal thin film. The resistance should be linear until a very low temperature and then turn constant [42]. Multiple similar measurements were made with different samples and the results were always similar.

There clearly has to be something wrong with the measurement of Figure 29. One possibility is that for some reason the sample is at a different temperature than the thermometer in the probe station. This would mean that there is some issue with the thermal contact of the sample and the cold finger, or that there is an issue with the cooling in the probe station. For some reason the system thermometer could be cooling faster than the sample which could create this curve. The other possibility is that this shape is created by some badly behaving contact resistance. This is a possibility since the contacts are mechanical probes. The hypothesis is that, as the temperature changes, so does the length of these metal probes, and this could create a changing contact resistance. This second issue could be testes by using a four probe measurement, which is not sensitive to contact resistances. So next a four probe measurement was done to a similar sample to study the effects of the contact resistance. Also the four probe measurement was more accurate since we measured the changes in the current directly.

The settings in the lock-in amplifier measuring the voltage were the same as in the two probe measurement, the settings for the lock-in amplifier measuring the current were sensitivity = 200 mV and time constant = 300 ms, with the preamplifier settings as explained in section 3.2.1. In Figure 30 the results of the four probe measurement are shown together, with the results of the two probe measurement for the same sample. Only the results collected while cooling are shown to make the figure clearer. It is immediately clear that the shapes of the curves are very similar, which means that the main problem

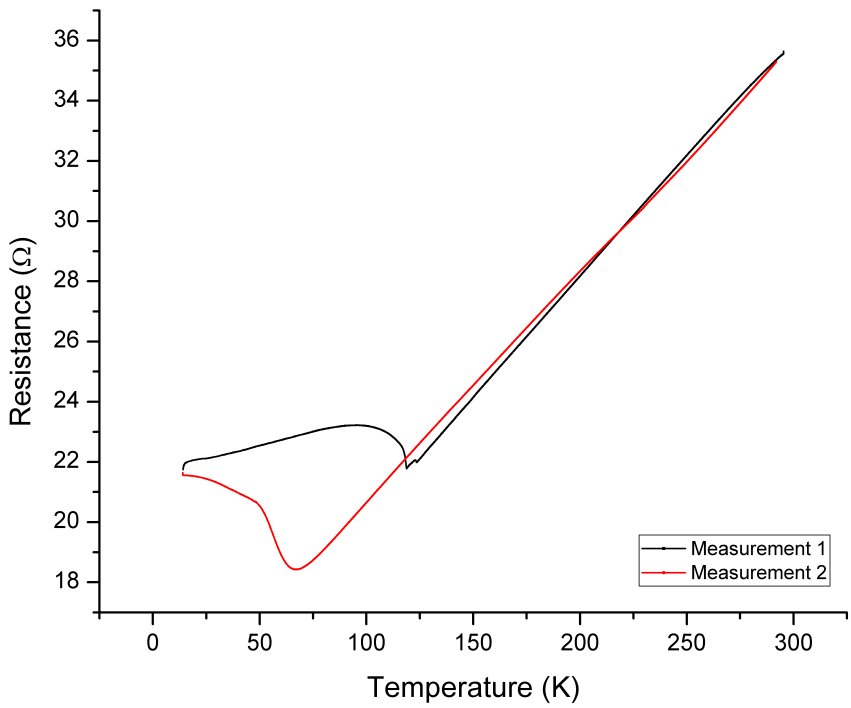

Figure 29: First solid wire heater/thermometer resistance measurement with the 2 probe setup. In measurement 1 the sample was cooling and in measurement 2 the sample was heating.

was not fixed with the four probe measurement setup. So the problem is not with the contact resistance of the probes. Figure 30 also shows, that the results are very similar at high temperatures, but at low temperatures there is an offset between the results, and also the weird shape starts at different temperatures. This fact suggests that the problem is indeed with the temperature measurement or the cooling of the probe station.

Even though at low temperatures there is an issue with the measurement, Figure 30 shows very nicely the difference between a two and a four probe measurement. In particular the inset curve shows that the results of the four probe measurement form a lot smoother curve. This is partially due to the fact that the four probe system is not sensitive to the differences in the contact resistance, which probably create the larger bumps in the curve of the two probe measurement. The four probe measurement also takes into account all the correlative peaks between the current and the voltage, and thus does not have the fluctuations seen in the two probe curve. In the two probe measurement this correlative noise could not be removed, because the current was assumed to be constant. Because of the clear advantages of the four probe measurement, all the later measurements were done with the four probe setups.

As mentioned before, after the four probe measurement it was clear that something was wrong with the temperature measurement in the probe station. We wanted to know what was actually happening in the station so we decided to measure a calibrated thermometer with the probe station. First I calibrated a Cernox thermometer (LakeShore CX-1030-BR-HT) using another already calibrated thermometer (LakeShore CX-1050-AA-1.4 L). For this calibration, I used the dip stick method shown in the experimental section and also explained in the next section. The calibration was done by measuring the resistances of both thermometers while they were cooled, by moving the dip stick closer to the

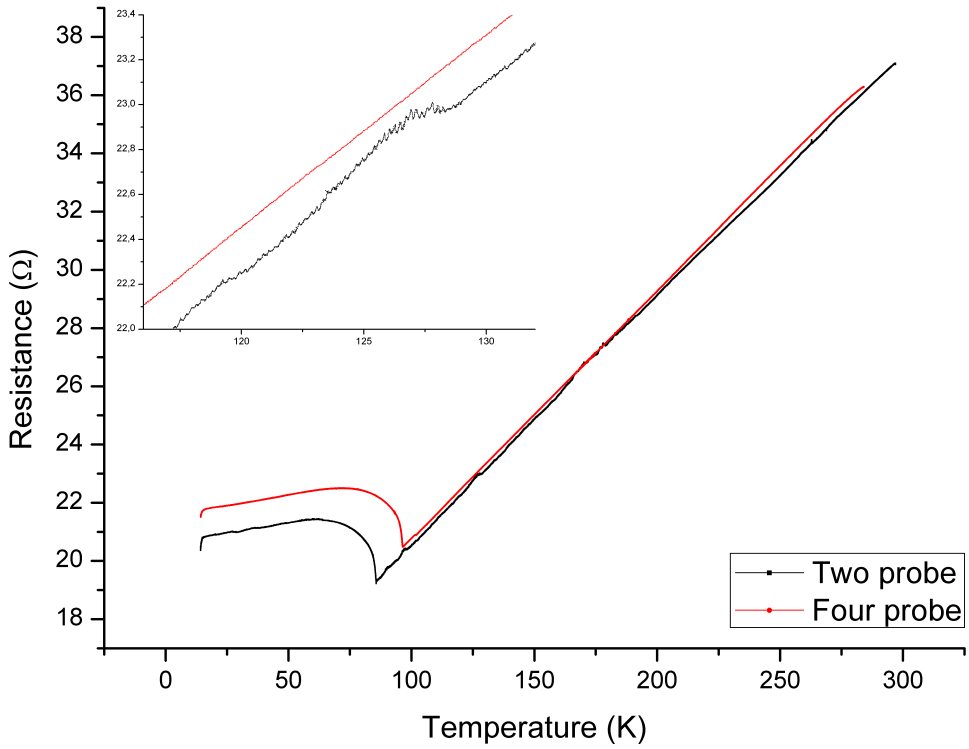

Figure 30: Comparison between a four probe and a two probe measurement for the same sample using the probe station.

liquid helium. After the calibration, the newly calibrated thermometer was set into the sample stage of the probe station the same way as all the measured samples. Then the resistance of the thermometer was measured with the exact same setup as the samples while the station was cooled. Finally, a curve was drawn which compares the temperatures measured by the probe station and the calibrated thermometer on the stage. This curve is the black curve in Figure 31. One can see that the curve is very similar in shape to the measurements done with the samples. What the figure tells us is that the temperature on the stage eventually saturates to a temperature of about 70 K while the thermometer in the probe station goes down to about 10 K.

The two possibilities are that either the thermometer in the probe station gives wrong values, or it is not well thermally connected to the stage and thus gives different values. It is quite unlikely that the thermometer would give wrong values, and we are led to conclude that the thermometers are actually at different temperatures. One possibility for this difference could be that there is something wrong with the radiation shield. It is possible for example that the window in the radiation shield lets some radiation in, which heats the thermometer on the sample stage. This was tested by shielding the windows and the thermometer on the stage with copper and aluminium tape, and doing a similar measurement. In addition to the added shielding, the measurement was done with a smaller excitation voltage of 0.070 V to make sure that the sample is not self-heating due to electric power. This measurement was done while the station was heating up, with the results shown as the red curve in Figure 31. It is clear that the added shielding did not help, and thus radiation is not the problem. Similarly, the lower voltage made no real difference as can be seen by comparing to Figure 29. These results leave basically only one conclusion: there is a bad thermal contact between the stage and the cold head

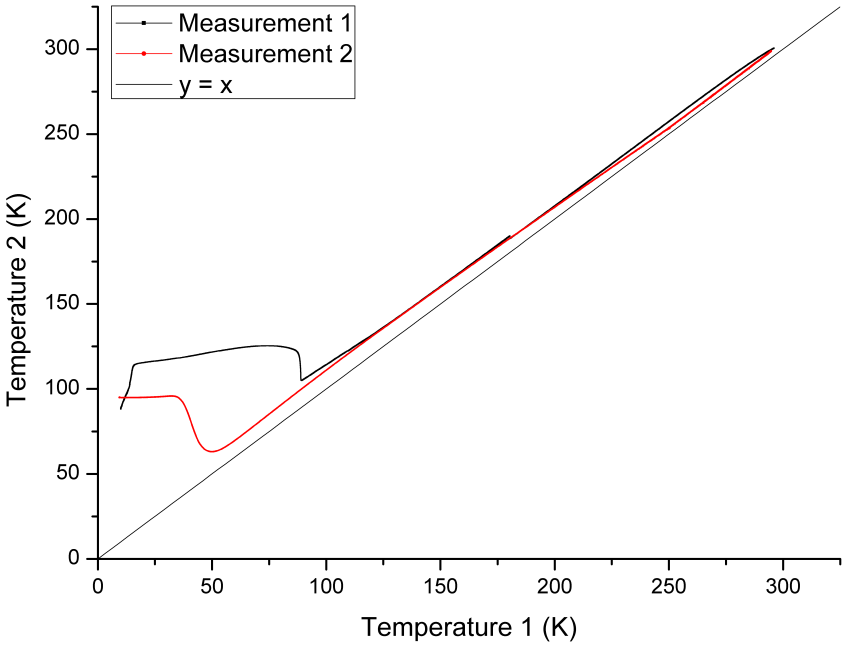

Figure 31: Comparison between the thermometer in the probe station (Temperature 1) and the calibrated thermometer on the sample stage (Temperture 2). Measurement 1 is without extra shielding while cooling, and measurement 2 is with extra shielding while heating.

where the thermometer of the probe station is. When looking at the graphs, it seems like the thermal contact is lost at around 100 K when cooling, and then comes back at around 50-60 K when the station is heated. This could be caused for example by thermal expansion in the thermal anchors. Whatever the reason the fact that the station is not working as it should meant that it could not be used for the measurements in the full temperature range. In fact this data shows a major design flaw in the whole probe station setup, which has to be communicated to the probe station company (Janis).

5.6 Dip stick measurements

Since it was clear that the probe station was giving wrong results, some other measurement setup had to be used to get the real resistance curves. The decision was made to use a dip stick setup which is a fast and an easy technique. This dip stick measurement was actually the only remaining option since I needed results from high temperatures as well, and most refrigerators at the Nanoscience Center only work at very low temperatures. In this setup, the sample is slowly lowered into liquid helium, and then slowly lifted up to get similar cooling and heating curves as with the probe station. A four probe setup was also used with this dip stick measurement. The circuit used for the measurement, as shown in section 3.2 was the same as with the probe station. The measurement was done to the same sample that was used for the probe station measurements in Figure 30. The settings for the lock-in amplifier measuring the voltage were the same as in the probe station measurement. For the lock-in amplifier measuring the current, the settings were sensitivity = 300 mV and time constant = 30 ms. The results of the dip stick measurement are shown in Figures 32 and 33. In Figure 32 the results of a cooling measurement for one sample are shown, along with the results from the probe station for comparison. In Figure 33 cooling and heating results for another sample are presented.

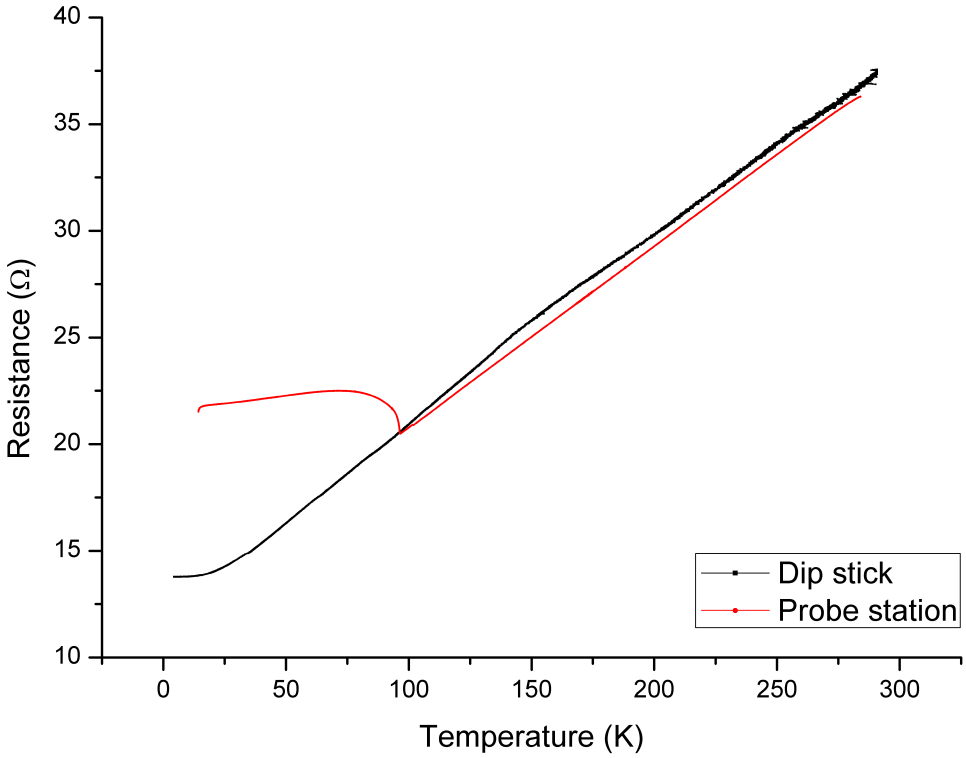

Figure 32: Results of the dip stick measurement compared with results using the probe station. Both measurements were done while cooling, using a four probe setup.

From both Figures 32 and 33 it is immediately clear that the results with the dip stick form a curve that has the correct shape. The shape is very similar to results obtained in other experiments [42]. When looking at Figure 32 the curve is different from the probe station measurement even in the linear section. This is expected based on the thermometer comparisons done with the probe station, as the probe station temperature does not accurately reflect the sample temperature. With the dip stick, both the cooling and heating curves are the same as Figure 33 shows. This means that there was no hysteresis, as there should not be. From the dip stick curve in Figure 33, also the temperature coefficient of resistance was determined by doing a least squares linear fit to the curve. The temperature coefficient can be calculated directly from the slope of the fitted line. The coefficients are usually given at a reference temperature, and the slope is just divided with the resistance at that temperature to get the coefficient. If 20 °C is the reference temperature, the slope has to be divided with the corresponding resistance which is 38.1848 Ω. This value had to be extrapolated from the linear fit. Then dividing the slope gives the coefficient for my sample which is $(2.36 * 10^{-3} \pm 3 * 10^{-5})$ K^{-1}. This is a bit smaller than some literature values for both gold and titanium which are $3.98 * 10^{-3}$ K^{-1} for gold and $5.5 * 10^{-3}$ K^{-1} for titanium [44]. The biggest difference between the literature values and my results arises from the fact that now we have a two metal wire, and also because this wire is actually a thin film with a thickness of about 70 nm. Also the amount of impurities in the metal affects the coefficient.

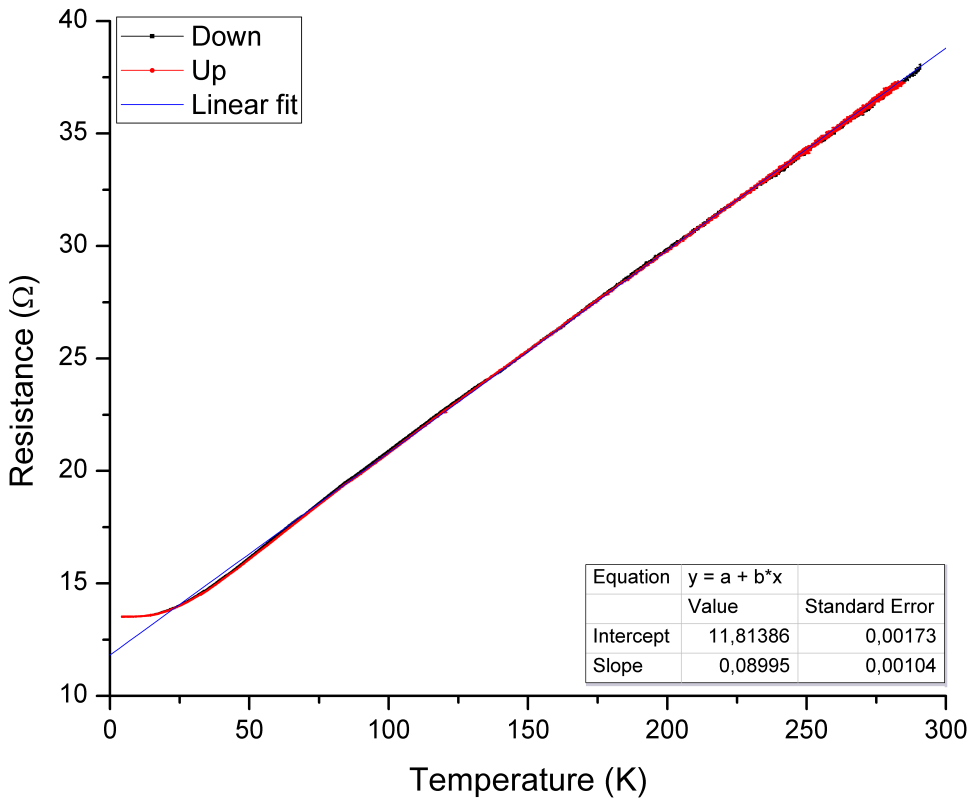

Figure 33: Cooling and heating curves for a sample measured with the dip stick method. Down means cooling, and up means heating. There is also a linear fit done to the cooling curve.

6 CONCLUSION

The first lithography tests already showed that the combination of the AR-P 3120 resist and Nanoscribe Photonic Professional with the air-gap objective can be used to do lithography in combination with metal deposition. With this process, metal lines with a width in below micron scale can be fabricated. In addition, when done just on the substrate, the lithography worked very well without any problems. This is clear when looking at Figures 17 and 18. The problems arose only when the process was transferred to do lithography on the already fabricated 3D base structures. The biggest problems were with the resist coating and the lift-off. The problem with the resist coating was that the resist did not stay on top of the structures. Because spray coating which might work on samples like this was not available, a workaround had to be used. This workaround was to fabricate small walls to hold the resist on the structure, with successful results, as is shown in Figure 22. The problem with the lift-off was that there was no resist on top of the small walls, which together with the fact that there is no undercut along the walls made the lift-off very difficult. There was always extra film left on the wall structures, and the structures often broke in the process, especially when using sonication. These problems were mostly fixed by the use of ALD to coat the structures with Al_2O_3 before the AR-P resist coating, and by making the small walls sloped on the inside, as shown in Figure 27. The process is still not perfected, however. The lift-off is still time consuming and hard, even with short bursts of sonication, and there can still be some extra gold film left on the structures. Also the process has to be done carefully, or the structures may break. So if this process is used in the future, it would be useful to develop it further.

In the resistance measurements, it was found that the four probe method with measurement of both voltage and current is better than the two probe method, which was of course expected. The difference between the methods is shown in Figure 30. The four probe method has better stability and it also leaves out the contact resistances. It was also found in the probe station measurements that there is an issue with the Janis probe station. After multiple tests, it was found that the problem is probably caused by the system losing the thermal contact between the sample stage and the cold head. This is best shown in Figure 31, where a thermometer on the stage was compared to the probe stations internal thermometer. The figure shows that while cooling, the temperature on the sample stage suddenly shoots up and while heating it suddenly drops down at one point. After this discovery, the measurements were done with the dip stick method. The results from these measurements agreed with results by other studies and showed that the fabricated wires can work as a heater and a thermometer, as a decent temperature coefficient was measured. The structures can work as a thermometer down to a temperature of about 25 K as can be seen from Figures 32 and 33. After this the resistance curve flattens out.

The process of making the two cuboid structures connected with small beams and then cutting with ion beam milling showed some promise. Gap sizes approaching sub-micron scale could be reached. With a simple design like this, a gap width of (1.97 ± 0.05) µm was reached. This is already smaller than the smallest gap that had been reached with

just the 3D lithography which was (2.2 ± 0.2) µm. However, the use of the beams caused the walls to bend pretty badly as can be seen from Figure 28. This could probably be fixed by connecting the structures with horizontal plates and then cutting them with the HIM. One could also make a completely connected structure and then create the whole gap with the HIM, but this would require a smaller structure and even then it would take a very long time to do. If time is not a problem, this would probably be the best way to create the gap because the resolution of the milling with neon is in the 10 nm range. The only problem with smaller structures is the smaller surface area of the parallel plates, which makes the heat transfer weaker and thus harder to detect. This could however be counteracted by getting the gap to be small enough.

If this project is to be continued, the next step should be finding out how heat is conducted through the structures. This could be done with a pretty simple 3-omega method measurement, which can be done by using the same wire as the heater and the thermometer at the same time. This kind of measurements have already been done with simple thin film wires by Tuomas Hänninen at the Nanoscience Center in Jyväskylä [45]. After it is known how the heat goes through the structure into the substrate, then one could move to the vacuum heat transfer measurements. Before this, a method for etching the substrate from between the samples needs to be found. This might be difficult with the sapphire substrates used here, and so maybe the structures will have to be fabricated onto silicon substrates. To get good results on the near field heat transfer one also needs to make the gap smaller. Luckily the ion beam milling showed great promise even in the preliminary experiment done in this study. I think that it would be possible to get a gap that is in the nanometre scale by making a new design for the structures, and then using milling to make the final gap.

REFERENCES

[1] M. P. Planck. *The Theory of Heat Radiation.* Blakiston's Son & Co., 1914.

[2] S. Basu et al. Review of near-field thermal radiation and its application to energy conversion. *Int. J. Energy Res.* 33: 1203–1232, 2009. DOI: 10.1002/er.1607.

[3] K. Ito et al. Parallel-plate submicron gap formed by micromachined low-density pillars for near-field radiative heat transfer. *Appl. Phys. Lett.* 106: 083504, 2015.

[4] Masahiro Nomura. Near-field radiative heat transfer: The heat through the gap. *Nature nanotechnology* 11: 496-497, 2016.

[5] R. St-Gelais et al. Near-field radiative heat transfer between parallel structures in the deep subwavelength regime. *Nature nanotechnology* letters 20, 2016.

[6] K. Kim et al. Radiative heat transfer in the extreme near field. *Nature* 528: 387-391, 2015.

[7] B. Song et al. Enhancement of near-field radiative heat transfer using polar dielectric thin films. *Nature nanotechnology* 10: 253–258, 2015.

[8] K. F. Chen et al. Suppressing sub-bandgap phonon–polariton heat transfer in near-field thermophotovoltaic devices for waste heat recovery. *Appl. Phys. Lett.* 107: 091106 2015.

[9] K. Ito et al. Parallel-plate submicron gap formed by micromachined low-density pillars for near-field radiative heat transfer. *Appl. Phys. Lett.* 106: 083504, 2015.

[10] B. Song et al. Radiative heat conductances between dielectric and metallic parallel plates with nanoscale gaps. *Nature nanotechnology* 11: 509–514, 2016.

[11] M. Laroche et al. Near-field thermophotovoltaic energy conversion. *J. Appl. Phys.* 100: 063704, 2006.

[12] O. Ilic et al. Overcoming the black body limit in plasmonic and graphene near-field thermophotovoltaic systems. *Opt. Express.* 20: A366–A384, 2012.

[13] C. R. Otey et al. Thermal rectification through vacuum. *Phys. Rev. Lett.* 104: 154301, 2010.

[14] P. Ben-Abdallah and S.-A. Biehs. Near-field thermal transistor. *Phys. Rev. Lett.* 112: 044301, 2014.

[15] Jean-Philippe Mulet et al. Enhanced radiative heat transfer at nanometric distances. *Microscale Thermophysical Engineering.* 6: 209–222, 2002.

[16] K. Joulain et al. Surface electromagnetic waves thermally excited: Radiative heat transfer, coherence properties and Casimir forces revisited in the near field. *Surface Science Reports.* 57: 59–112, 2005.

[17] H.-B. Sun and S. Kawata. Two-photon photopolymerization and 3D lithographic microfabrication. *Advances in Polymer Science*, Volume 170:169-273, Springer, 2004.

[18] S. Katawa et al. Finer features for functional microdevices. *Nature.* 412: 697-698, 2001. DOI: 10.1038/35089130.

[19] Samuli T. Heiskanen. Rakorakenteen valmistaminen 3D-litografian avulla. *Bachelor thesis, University of Jyväskylä.* 2014.

[20] Samuli T. Heiskanen. Structure design and fabrication for near field heat transfer. *Special assignment, University of Jyväskylä.* 2015.

[21] R. Hill et al. Helium ion microscopy. *Advances in Imaging and Electron Physics.* 170: 65-148, 2012.

[22] Z. Geng et al. Development of an Inductive NIS Thermometer. *J. Phys.: Conf. Ser.* 400: 052005, 2012.

[23] J. Weber. Fluctuation dissipation theorem. *Phys. Rev.* 101: 1620-1626, 1956.

[24] J. E. Sipe, New Green-Function Formalism for Surface Optics, J. Opt. Soc. Am. B, vol. 4, p. 481, 1987.

[25] P.-O. Chapuis et al. Effects of spatial dispersion in near-field radiative heat transfer between two parallel metallic surfaces. *Phys. Rev. B* 77: 035431, 2008.

[26] Polder and M. Van Hove, Theory of Radiative Heat Transfer between Closely Spaced Bodies, Phys. Rev. B, vol. 4, p. 3303, 1971.

[27] Y. R. Shen. The Principles of Nonlinear Optics. Wiley Classics Library, 1984.

[28] S. Cabrini and S. Kawata. *Nanofabrication Handbook.* CRC Press, 2012.

[29] M. Bass. *Handbook of Optics*, Vol. I, 2nd edition. McGraw-Hill, Inc, 1995.

[30] B.H. Cumpston et al. Two-photon polymerization initiators for three-dimensional optical data storage and microfabrication. *Nature.* 398: 51-54,1999. DOI: 10.1038/17989.

[31] K. Dorkenoo et al. Monitoring the Contractile Properties of Optically Patterned Liquid Crystal Based Elastomers. *Advanced Elastomers: Technology, Properties and Applications.* Editor Anna Boczkowska. InTech, 2012.

[32] Riikka L. Puurunen. Surface chemistry of atomic layer deposition: A case study for the trimethylaluminum/water process. *Journal of Applied Physics.* 97, 121301, 2005. DOI: 10.1063/1.1940727.

[33] Steven M. George. Atomic Layer Deposition: An Overview. *Chemical Reviews.* 110, 111–131, 2010. DOI: 10.1021/cr900056b.

[34] S.M. George et al. Surface Chemistry for Atomic Layer Growth. *J. Phys. Chem.* 1996, 100, 13121.

[35] Y. Widjaja and C.B. Musgrave. Quantum chemical study of the mechanism of aluminum oxide atomic layer deposition. *Appl. Phys. Lett.* 80: 3304-3306, 2002.

[36] Noel M. Dawson. Atomic layer deposition of aluminum oxide. *Bachelor thesis, University of California, Santa Cruz.* 2010.

[37] Sami Franssila. *Introduction to Microfabrication*, 2nd edition. Wiley, 2010.

[38] http://www.frontiersinoptics.com/home/about-fio-ls/the-fio-blog-luminous-insights/2013/october-2013/nano-scale-artistic-work-–-ultra-fine-3d-structure/. Cited 29.9.2016.

[39] P. Yimsiria and M.R. Mackley. Spin and dip coating of light-emitting polymer solutions: Matching experiment with modelling. *Chemical Engineering Science* 61: 3496-3505, 2006.

[40] Jaakko Mastomäki.3D-litografian optimointi ilmarako-objektiivilla käyttäen positiivista resistiä. *Bachelor thesis, University of Jyväskylä.* 2015.

[41] http://www.nanoscribe.de/en/products/ip-photoresists/. Cited 26.11.2016.

[42] J.W.C. de Vries. Resistivity of thin Au films as a function of grain diameter and temoperature. *J. Phys. F: Met. Phys.* 17: 1945-1952, 1987.

[43] K.A. Cooper et al. Conformal photoresist coatings for high aspect ratio features. *SUSS MicroTec Waterbury Center.* VT, USA. 2007.

[44] M. Kervinen et al. *Maol taulukot*, 2nd edition. Otava Oy, 2006.

[45] Tuomas Hänninen. Implementing the 3-Omega Technique for Thermal Conductivity Measurements. *Pro Gradu, University of Jyväskylä.* 2013.